# Experimental studies of the NaCs $5^3\Pi_0$ and $1(a)^3\Sigma^+$ states

S. Ashman,[a] B. McGeehan,[b] C. M. Wolfe,[c] C. Faust, K. Richter, J. Jones, A. P. Hickman, and J. Huennekens[d]
*Department of Physics, 16 Memorial Dr. East, Lehigh University, Bethlehem, Pennsylvania 18015, USA*

(Received 14 November 2011; accepted 8 February 2012; published online 21 March 2012)

We report high resolution measurements of 372 NaCs $5^3\Pi_0(v, J)$ ro-vibrational level energies in the range $0 \leq v \leq 22$. The data have been used to construct NaCs $5^3\Pi_0$ potential energy curves using the Rydberg–Klein-Rees and inverted perturbation approximation methods. Bound-free $5^3\Pi_0(v, J) \rightarrow 1(a)^3\Sigma^+$ emission has also been measured, and is used to determine the repulsive wall of the $1(a)^3\Sigma^+$ state and the $5^3\Pi_0 \rightarrow 1(a)^3\Sigma^+$ relative transition dipole moment function. Hyperfine structure in the $5^3\Pi_0$ state has not been observed in this experiment. This null result is explained using a simple vector coupling model. © *2012 American Institute of Physics*. [http://dx.doi.org/10.1063/1.3689388]

## I. INTRODUCTION

Alkali molecules are currently of great interest due to recent progress in production and trapping of ultracold species.[1–26] Heteronuclear alkali-metal diatomics have recently drawn particular attention because each molecule has a permanent electric dipole moment, allowing for manipulation by an external electric field. In principle, these molecules can be oriented in a trap or optical lattice, and so they are also of interest in proposed quantum computing schemes.[27–30] In addition, the polarity of these molecules may be of interest for controlled chemical reactions. Polar diatomics (especially in $^1\Pi$ states) might also be used for sensitive, noncontact mapping of external electric field distributions via changes in laser induced fluorescence caused by parity mixing due to the quasilinear Stark effect.[31] Because of these important potential applications, there is a great need for experimental spectroscopic studies of the heteronuclear alkali diatomics to map out potential energy curves, investigate spin-orbit interactions and hyperfine structures, and determine transition and permanent dipole moments. Such measurements provide necessary data for the planning and interpretation of experiments involving creation and trapping of ultracold polar molecules and also provide stringent tests of state-of-the-art theoretical calculations.

Much of our previous work has involved the NaK molecule, which has served as an ideal laboratory for the study of various excited potential energy curves and transition dipole moment functions, spin-orbit and non-adiabatic coupling between states, and fine and hyperfine structure in different angular momentum coupling limits (as well as intermediate cases).[32–45] However, various technical factors favor the use of NaCs or RbCs rather than NaK for ultracold molecule applications, while the little studied LiCs molecule[46] may also be attractive since it has the largest permanent dipole moment of any alkali molecule.

The NaCs molecule, which has the second largest permanent dipole moment of all alkali diatomics, was first studied in high resolution by Onomichi and Katô[47] and Diemer *et al.*[48] The ground state was mapped with high accuracy by Docenko *et al.*[12,49] and a recent detailed study by Zaharova *et al.*[50] has unraveled the important $A^1\Sigma^+ \sim b^3\Pi$ manifold whose levels serve as the intermediate state in the double-resonance work described here. The work of Zaharova *et al.* highlights the formidible challenges of studying the heavier alkali molecules. Level spacings are much smaller than in lighter molecules (resulting in simultaneous pumping of multiple levels), and spin-orbit interaction constants are much larger (resulting in widespread and large perturbations that significantly complicate the process of assigning lines).

In the present work, we report the first study of the NaCs $5^3\Pi_0$ state, which correlates adiabatically to the $Na(3S_{1/2}) + Cs(6D_{5/2})$ separated atom limit. We measured the energies of 401 $5^3\Pi_0(v, J)$ levels in the range $v = 0$–34, and used the energies of levels in the range $v = 0$–22 to construct a $5^3\Pi_0$ potential energy curve using the inverted perturbation approximation (IPA) method.[51] $5^3\Pi_0(v, J)$ levels are detected by their bright green bound-free fluorescence to the mostly repulsive $1(a)^3\Sigma^+$ state. Comparison of the resolved $5^3\Pi_0(v, J) \rightarrow 1(a)^3\Sigma^+$ bound-free fluorescence with simulated spectra allowed us to map the $1(a)^3\Sigma^+$ state repulsive wall and the $5^3\Pi_0 \rightarrow 1(a)^3\Sigma^+$ relative transition dipole moment function.

This paper is organized as follows. In Sec. II, we describe the experimental setup and the experimental technique. Section III reports our analysis and results for the NaCs $5^3\Pi_0$ state. Section IV describes our fitting of the NaCs $1(a)^3\Sigma^+$ repulsive wall and the $5^3\Pi_0 \rightarrow 1(a)^3\Sigma^+$ relative transition dipole moment function by comparison of resolved, bound-free $5^3\Pi_0(v, J) \rightarrow 1(a)^3\Sigma^+$ fluorescence to simulated spectra. Section V presents a discussion of hyperfine structure in

[a]Present address: Department of Physics and Astronomy, University of Wisconsin–Stevens Point, Stevens Point, Wisconsin 54481, USA.
[b]Present address: Epic Systems Corp., 1979 Milky Way, Verona, Wisconsin 53593, USA.
[c]Present address: RDRL-WMP-A, Aberdeen Proving Ground, Maryland 21005-5066, USA.
[d]Author to whom correspondence should be addressed. Electronic mail: jph7@lehigh.edu.

 

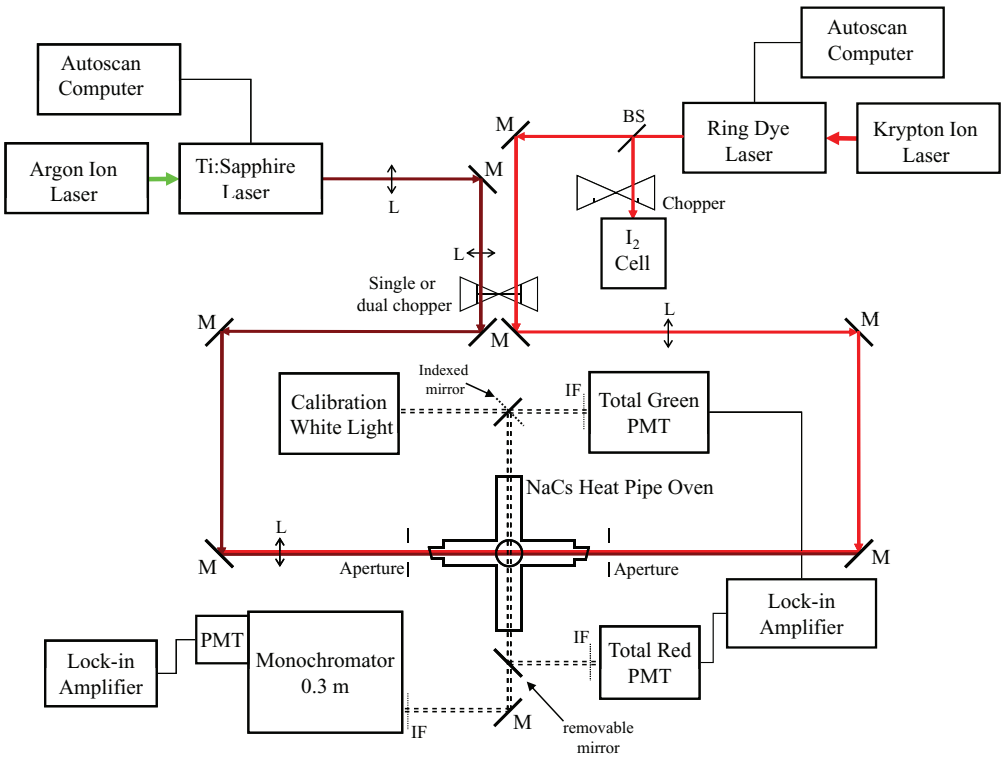


FIG. 1. Experimental setup. M is mirror, BS is beam splitter, IF is interference filter, L is lens, and PMT is photomultiplier tube.

Hund's cases *a* and *c* and explains why we don't observe such structure for the NaCs $5^3\Pi_0$ state in the current experiment. Our conclusions appear in Sec. VI.

## II. THE EXPERIMENT

Our experimental approach is derived from the optical–optical double resonance (OODR) method,[34,35,52–69] which has proven itself to be one of the most versatile and robust techniques of high-resolution laser spectroscopy. When narrow-band cw lasers are employed, this technique is inherently Doppler-free, so that very high resolution excitation spectra can be obtained. Extensive work has concentrated on the homonuclear alkali molecules,[52–65] while heteronuclear alkali molecules[34,35,66–69] have received somewhat less attention. Most studies have investigated high-lying singlet electronic states, due to the dipole selection rule on spin, $\Delta S = 0$, and the fact that the electronic ground state of all alkali molecules is a spin singlet ($S = 0$). Triplet states can be probed by a variant of OODR called "perturbation-facilitated optical–optical double resonance" (PFOODR).[70–90] This method relies on the existence of perturbations that can couple specific ro-vibrational levels of singlet and triplet electronic states, most notably the $b^3\Pi$ and $A^1\Sigma^+$ states. These perturbed or mixed levels act as "windows" into the triplet manifold. The cw PFOODR technique has allowed study of the hyperfine structure of many triplet electronic states of $Li_2$,[74–78] $Na_2$,[78–85] and $K_2$.[90] In general, much less is known about the heteronuclear alkali diatomic triplet states, although several studies of NaK,[36–41,91,92] and a few studies of NaRb,[93,94] KRb,[95,96] RbCs,[97] and NaCs[26,50] have been carried out.

The experimental setup is shown in Fig. 1 and is similar to that used in our previous work on NaK.[37–40,98] A mixture of sodium and cesium was heated in a five-arm, stainless steel heat pipe oven, to a temperature in the range 290–320 °C, creating a vapor of NaCs, $Na_2$, and $Cs_2$ molecules as well as Na and Cs atoms. Argon at a pressure 3.0–5.0 Torr was used as a buffer gas to protect the oven windows from the corrosive metal vapor.

NaCs molecules were excited to the $5^3\Pi_0$ state using the PFOODR technique (see Fig. 2). The pump laser is a Coherent model 899-29 single-mode Titanium-Sapphire laser pumped by a 10 W argon ion laser. Its frequency was tuned to line-center of a particular NaCs $1(b)^3\Pi_0(v_b, J') \sim 2(A)^1\Sigma^+(v_A, J') \leftarrow 1(X)^1\Sigma^+(v'', J'' = J' \pm 1)$ transition, where the upper $1(b)^3\Pi_0(v_b, J') \sim 2(A)^1\Sigma^+(v_A, J')$ level has mixed singlet and triplet character due to the strong spin-orbit coupling in this heavy molecule. Pump laser transitions used in the present work are listed in Table 1 of the supplementary materials.[99] The probe laser is a Coherent 699-29 single-mode dye laser, using LD700 dye, which is pumped by 3–5 W from a krypton ion laser. The probe laser was used to further excite the NaCs molecules from the intermediate $1(b)^3\Pi_0(v_b, J') \sim 2(A)^1\Sigma^+(v_A, J')$ level to various $5^3\Pi_0(v, J = J' \pm 1)$ levels: $5^3\Pi_0(v, J = J' \pm 1) \leftarrow 1(b)^3\Pi_0(v_b, J') \sim 2(A)^1\Sigma^+(v_A, J')$. Typical dye and Ti:Sapphire laser powers are 200–600 mW and 150–600 mW, respectively. The dye and Ti:Sapphire lasers counter-propagated through the oven, and were carefully overlapped at the center of the heat pipe, with spot sizes of ~1 mm. Dye laser frequencies were calibrated by comparing laser-induced fluorescence from an iodine cell with lines listed in the $I_2$ spectral atlas,[100] while Ti:Sapphire laser

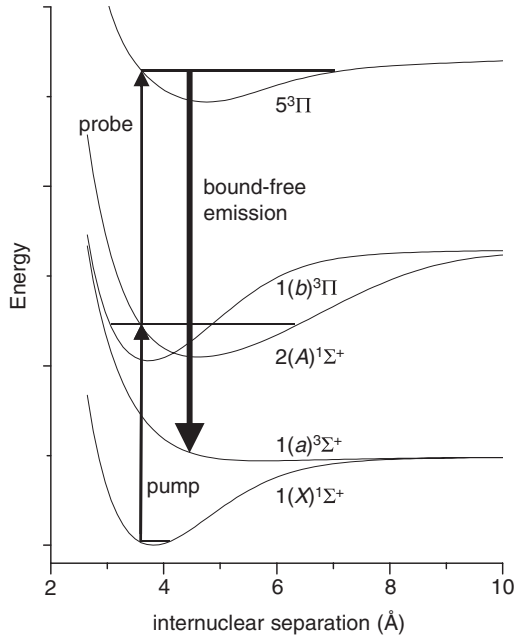


FIG. 2. PFOODR pump and probe scheme used to study the NaCs $5^3\Pi_0$ and $1(a)^3\Sigma^+$ states. The thick downward arrow indicates the $5^3\Pi_0 \rightarrow 1(a)^3\Sigma^+$ bound-free emission.

frequencies were calibrated using optogalvanic spectra from a uranium hollow cathode lamp. We believe that $5^3\Pi_0$ level energies are determined to within an absolute accuracy of $\sim 0.02\ \text{cm}^{-1}$.

Fluorescence emitted perpendicular to the laser propagation direction was collected using three detectors (see Fig. 1). A red-filtered (700–1000 nm bandpass filters) free-standing PMT (Hamamatsu R406) monitors $2(A)^1\Sigma^+(v_A, J') \rightarrow 1(X)^1\Sigma^+$ fluorescence, and was used to set the pump laser to line-center of a selected $1(b)^3\Pi_0(v_b, J') \sim 2(A)^1\Sigma^+(v_A, J') \leftarrow 1(X)^1\Sigma^+(v'', J'' = J' \pm 1)$ transition. A green/violet filtered (575, 650, 675, and 700 nm shortpass filters) free-standing PMT (Hamamatsu R928) was used to detect $5^3\Pi_0 \rightarrow 1(a)^3\Sigma^+$ bound-free continuum fluorescence as the probe laser was scanned over the various $5^3\Pi_0(v, J = J' \pm 1) \leftarrow 1(b)^3\Pi_0(v_b, J') \sim 2(A)^1\Sigma^+(v_A, J')$ transitions (excitation spectra). Because the narrow-band pump laser only excites molecules in one specific velocity group, the OODR method is intrinsically Doppler-free, and homogeneous linewidths can be resolved. Finally, a monochromator/PMT system (McPherson model 218 with 0.53 nm resolution and Hamamatsu R1387) was used to record resolved fluorescence when the pump and probe laser frequencies were fixed to pump a particular $5^3\Pi_0(v, J = J' \pm 1) \leftarrow 1(b)^3\Pi_0(v_b, J') \sim 2(A)^1\Sigma^+(v_A, J') \leftarrow 1(X)^1\Sigma^+(v'', J'' = J' \pm 1)$ OODR transition (375–550 nm bandpass filters were used here). The monochromator wavelength scale was calibrated using known mercury atomic lines.[101] In all cases, the pump laser was modulated with a mechanical chopper, and lock-in detection was employed.

The relative intensity vs. wavelength in the resolved fluorescence spectra was used to determine the relative transition dipole moment function (see Sec. IV). Therefore, the resolved spectra were corrected for the relative wavelength-dependent detection system efficiency using a calibrated white light.[102] In addition, slight variations in the laser intensities or beam overlap could result in systematic changes in the strength of the OODR pumping during the time required to complete a resolved scan. To monitor this, the total $5^3\Pi_0 \rightarrow 1(a)^3\Sigma^+$ bound-free continuum fluorescence was continuously recorded by the green/violet detector as each resolved fluorescence scan was taken. If the total $5^3\Pi_0 \rightarrow 1(a)^3\Sigma^+$ bound-free fluorescence signal varied more than 5–10% over the scan duration, the scan was rejected.

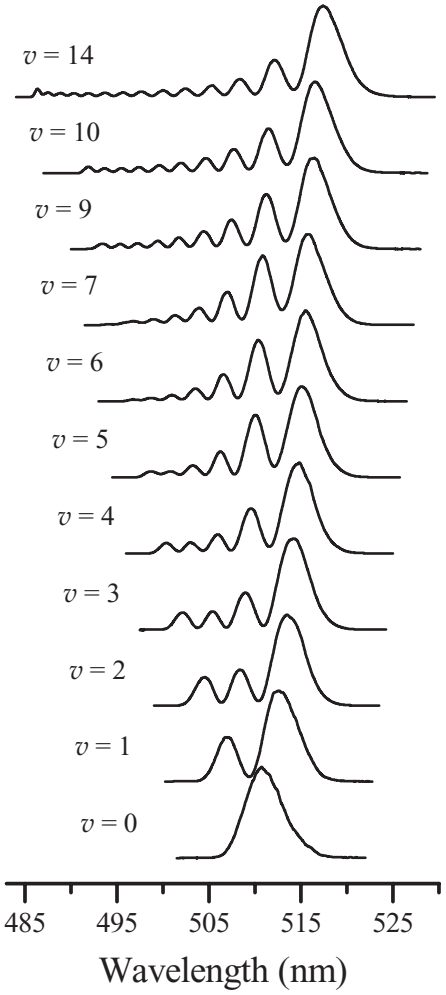


FIG. 3. NaCs $5^3\Pi_0(v, J) \rightarrow 1(a)^3\Sigma^+$ bound-free emission spectra for $(v, J) = (0, 31)$, (1, 25), (2, 25), (3, 43), (4, 33), (5, 33), (6, 45), (7, 31), (9, 33), (10, 31), and (14, 31). Only $v$ is used to label the scans in the figure since the bound-free emission depends only weakly on $J$.

We have not yet observed hyperfine structure in any excited state levels of NaCs. We believe this is due to the fact that most states of NaCs are expected to follow Hund's case $c$ angular momentum coupling scheme (see Sec. V below). Consequently, all observed double resonance excitation lines appear as single structureless peaks, regardless of the upper electronic state. Therefore, we had to use the resolved fluorescence pattern to identify the electronic states involved. Several different patterns were observed, but $5^3\Pi_0$ levels could be easily identified by the characteristic bound-free $5^3\Pi_0 \rightarrow 1(a)^3\Sigma^+$ fluorescence pattern shown in Fig. 3. The identification of the observed levels as belonging to the $5^3\Pi_0$ elec-

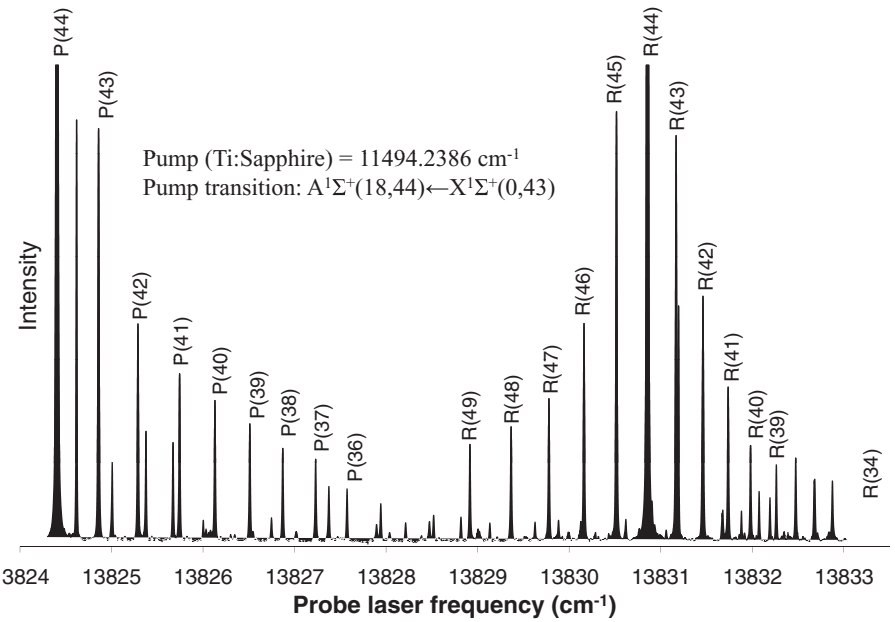


FIG. 4. Collisional lines observed using the OODR technique with the pump laser frequency fixed on the $1(b)^3\Pi_0(v_b, J = 44) \sim 2(A)^1\Sigma^+(v_A = 18, J = 44) \leftarrow 1(X)^1\Sigma^+(v_X = 0, J = 43)$ transition while the probe laser frequency is scanned. The direct probe transitions $5^3\Pi_0(v = 16, J = 43, 45) \leftarrow 1(b)^3\Pi_0(v_b, J = 44) \sim 2(A)^1\Sigma^+(v_A = 18, J = 44)$ (labeled *P*(44) and *R*(44) in the spectrum) extend far off-scale. A series of collisional lines adjacent to each direct line is clearly visible, and it can be seen that rates for collisional population transfer fall monotonically with increasing $|\Delta J|$.

tronic state was based upon the strong bound-free emission to the $1(a)^3\Sigma^+$ state (confirming the upper state as triplet) and the good agreement between the observed and predicted vibrational and rotational level splittings. As we will see below, this assignment is also confirmed by the good agreement between the observed and predicted $5^3\Pi_0(v, J) \rightarrow 1(a)^3\Sigma^+$ bound-free fluorescence patterns, and between the experimentally measured $5^3\Pi_0 \rightarrow 1(a)^3\Sigma^+$ relative transition dipole moment function and theory.

Using the Ti:Sapphire laser and the dye laser with the PFOODR technique, we were able to access a region spanning approximately 23 900–29 000 $cm^{-1}$ in total energy as measured from the bottom of the ground state potential well, where the higher end of this energy range requires pump transitions from the ground state $v'' = 5$–10 levels. This energy region spans a large portion of the $5^3\Pi_0$ electronic state, including the bottom of the potential, and we were able to observe vibrational levels down to $v = 0$.

The data field was greatly expanded by including collisional satellite lines, which were often observed as a regular array of weak lines flanking the strong direct line (see Fig. 4). These lines result from collisional transfer of population in the intermediate state (see Fig. 5(b)); i.e., $2(A)^1\Sigma^+(v_A, J') + (\text{Ar, Cs}) \rightarrow 2(A)^1\Sigma^+(v_A, J' + \Delta J) + (\text{Ar, Cs})$, followed by probe laser excitation $5^3\Pi_0(v, J = J' + \Delta J \pm 1) \leftarrow 1(b)^3\Pi_0(v_b, J' + \Delta J) \sim 2(A)^1\Sigma^+(v_A, J' + \Delta J)$. A two step process, shown schematically in Fig. 5, allowed us to measure the energy of each upper "collisional" $5^3\Pi_0(v, J = J' + \Delta J \pm 1)$ ro-vibrational level relative to the well known ground state levels[49] with the same accuracy as for the direct lines. First, we observed total $5^3\Pi_0 \rightarrow 1(a)^3\Sigma^+$ green fluorescence with the probe laser frequency fixed on a particular $5^3\Pi_0(v, J = J' \pm 1) \leftarrow 1(b)^3\Pi_0(v_b, J') \sim 2(A)^1\Sigma^+(v_A, J')$ transition while the pump laser wavelength was scanned over a series of $1(b)^3\Pi_0(v_b, J') \sim 2(A)^1\Sigma^+(v_A, J') \leftarrow 1(X)^1\Sigma^+(v'', J'' = J' \pm 1)$ transitions (direct lines) and $1(b)^3\Pi_0(v_b, J' + \Delta J) \sim 2(A)^1\Sigma^+(v_A, J' + \Delta J) \leftarrow 1(X)^1\Sigma^+(v'', J'' = J' + \Delta J \pm 1)$ transitions (collisional lines) (Fig. 5(a)). In this case, the pump laser frequency associated with each transition provides a direct measure of the true intermediate $1(b)^3\Pi_0(v_b, J' + \Delta J) \sim 2(A)^1\Sigma^+(v_A, J' + \Delta J)$ level energy relative to the known ground state $1(X)^1\Sigma^+(v'', J'' = J' + \Delta J \pm 1)$ level energy, even though these intermediate state levels may be strongly perturbed. In step two (Fig. 5(b)), the roles of the two lasers were reversed. The pump laser frequency was fixed on a single $1(b)^3\Pi_0(v_b, J') \sim 2(A)^1\Sigma^+(v_A, J') \leftarrow 1(X)^1\Sigma^+(v'', J'' = J' \pm 1)$ transition while the probe laser frequency was scanned over $5^3\Pi_0(v, J = J' \pm 1) \leftarrow 1(b)^3\Pi_0(v_b, J') \sim 2(A)^1\Sigma^+(v_A, J')$ transitions (direct lines) and $5^3\Pi_0(v, J = J' + \Delta J \pm 1) \leftarrow 1(b)^3\Pi_0(v_b, J' + \Delta J) \sim 2(A)^1\Sigma^+(v_A, J' + \Delta J)$ transitions (collisional lines). Here, the probe laser frequency associated with each transition provides a direct measure of the upper $5^3\Pi_0(v, J = J' + \Delta J \pm 1)$ level energy relative to the previously determined intermediate level energies. An example of one of these "collisional spectra" is shown in Fig. 4.

Such collisional progressions provide data on a great number of rotational levels within a single vibrational state. Note that once a particular range of intermediate state levels had been mapped out, it was easy to shift both the initial $J''$ and final $J'$ values of the pump transition by ~10–15 and then map out another set of rotational levels centered on the new direct line. Note also that rotational quantum number assignments were easily confirmed by observing the same $5^3\Pi_0(v, J = J' \pm 1) \leftarrow 1(b)^3\Pi_0(v_b, J') \sim 2(A)^1\Sigma^+(v_A, J')$ probe transition when pumping the intermediate level $1(b)^3\Pi_0(v_b, J') \sim 2(A)^1\Sigma^+(v_A, J')$ from each of the two ground state levels

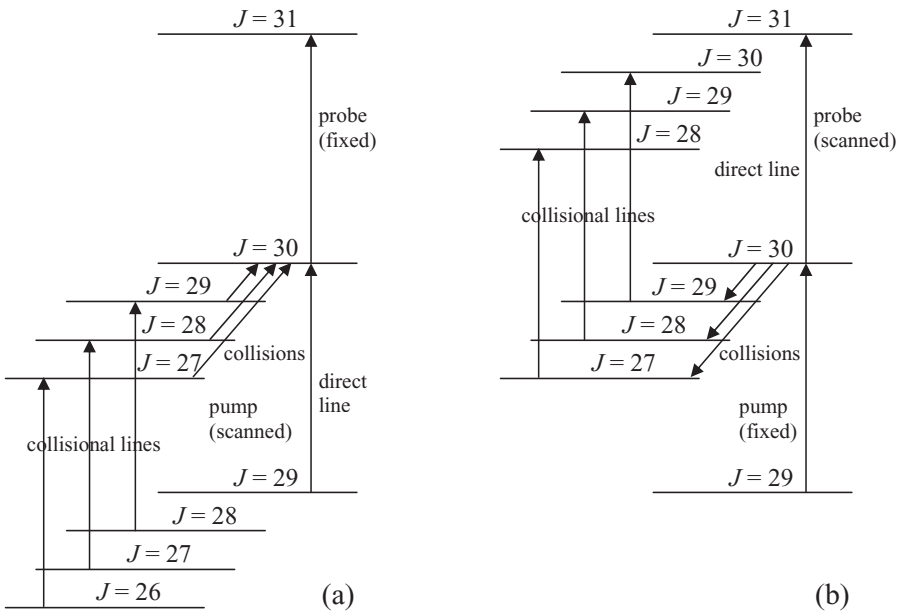


FIG. 5. Schematic diagrams showing the technique for using collisional lines to measure NaCs $5^3\Pi_0$ ro-vibrational level energies relative to known $1(X)^1\Sigma^+$ level energies. In (a), the pump frequency is scanned while the probe frequency is fixed. Pump laser frequencies corresponding to the observed collisional lines determine intermediate $1(b)^3\Pi_0(v_b, J) \sim 2(A)^1\Sigma^+(v_A, J)$ level energies relative to known ground state energies. In (b), the probe frequency is scanned while the pump frequency is fixed. Probe frequencies corresponding to the observed collisional lines determine $5^3\Pi_0(v, J)$ level energies relative to the $1(b)^3\Pi_0(v_b, J) \sim 2(A)^1\Sigma^+(v_A, J)$ level energies.

$1(X)^1\Sigma^+(v'', J'' = J' + 1)$ and $1(X)^1\Sigma^+(v'', J'' = J' - 1)$. If the assignment is correct, the difference between these two pump transition frequencies must exactly match the known energy separation between the two ground state levels, regardless of whether the intermediate level is perturbed.

Vibrational assignments of $5^3\Pi_0(v, J)$ levels were made by counting the nodes in the bound-free fluorescence spectra (see Fig. 3). However, a careful examination of the data (including the scans shown in Fig. 3) reveals that the experimental resolution is such that one node of the bound-free emission spectra at the short wavelength end is washed out in going from $v = 6$ to $v = 7$. For all higher $v$'s, the node count in the experimental spectra is one unit too small. Simulations first lose one node at $v \approx 14$.

We observed $5^3\Pi_0$ ro-vibrational levels with $v = 0$–12, 14–20, 22, 27, 29, and 32–34. The full set of observed ro-vibrational levels can be found in Table 2 of the supplementary materials.[99] However, we consider assignments above $v = 22$ to be tentative because the data in that range were sparse. For this reason, only the data in the range $v = 0$–22 were used to construct the $5^3\Pi_0$ potential energy curve (see Sec. III).

## III. ANALYSIS AND RESULTS FOR THE NaCs $5^3\Pi_0$ STATE

### A. Dunham Coefficients and $5^3\Pi_0$ Rydberg–Klein-Rees Potential Curve

In total, we measured 794 NaCs $5^3\Pi_0(v, J = J' \pm 1) \leftarrow 1(b)^3\Pi_0(v_b, J') \sim 2(A)^1\Sigma^+(v_A, J')$ transition frequencies, representing 598 different probe laser transitions (some transitions were measured more than once or with different pump transitions) and 401 different $5^3\Pi_0(v, J)$ levels in the range $v = 0$–34. These transitions are all listed in Table 2 of the supplementary materials.[99] The coverage in the range $v = 23$–34 is very sparse, so the remainder of the analysis and construction of the potential energy curve was limited to the 743 measurements of $5^3\Pi_0(v, J)$ level energies [representing 372 different $5^3\Pi_0(v, J)$ levels] with $v$ in the range 0–22. We carried out a least squares fit of 722 (359 different $5^3\Pi_0(v, J)$ levels) of these 743 measured ro-vibrational energies to the Dunham expansion,

$$E(v, J) = \sum_{i,k} Y_{ik} \left(v + \tfrac{1}{2}\right)^i [J(J+1) - \Omega^2]^k, \qquad (1)$$

using the program DParFit.[103] Note that here, $\Omega = 0$. The $(v, J)$ levels (5, 29), (5, 43), (8, 59–64), (9, 45), (10, 11), (10, 45), (16, 21), and (16, 25) were excluded from the fit, either because we were uncertain of the assignment, or because the level appeared to be locally perturbed.

The Dunham coefficients obtained in the fit are listed in Table I. The value of the centrifugal distortion constant $Y_{02}$ was fixed at the value $Y_{02} = -D_v = -7.2 \times 10^{-8}$ cm$^{-1}$. This was the average value obtained from fits of the expression $E(v, J) = G_v + B_v J(J+1) - D_v[J(J+1)]^2$ to the rotational level energies in the $v = 6$, 10, 16, and 17 levels, for which long rotational progressions had been measured. The RMS deviation of fitted level energies from the measured energies is 1.17 cm$^{-1}$. Inclusion of additional rotational terms, $Y_{21}$ and $Y_{31}$, did not significantly improve the fit (RMS deviation dropped to 1.14 cm$^{-1}$), so these terms are not reported. We note that the poor quality of the Dunham fit is due to the fact that both the rotational constant, $B_v$, and the vibrational splitting, $\Delta G_v$, are oscillatory functions of $v$ (see Ref. 104 and Fig. 6), indicative of global perturbations by nearby electronic states affecting a large range of rotational levels in a given vi-

TABLE I. Dunham coefficients obtained from fit of NaCs $5^3\Pi_0(v, J)$ level energies in the range $0 \le v \le 22$ to the Dunham expansion, Eq. (1). All values are in $cm^{-1}$. The centrifugal distortion term, Y(0, 2), was fixed at the value $-7.2 \times 10^{-8}$ $cm^{-1}$.

| | Experiment (this work) | Theory[106] |
|---|---|---|
| Y(0,0) | $24511.79 \pm 0.89$ | 24 578[a] |
| Y(1,0) | $64.24 \pm 0.43$ | 58.6 |
| Y(2,0) | $-1.750 \pm 0.068$ | ... |
| Y(3,0) | $0.1060 \pm 0.0041$ | ... |
| Y(4,0) | $-(2.211 \pm 0.085) \times 10^{-3}$ | ... |
| Y(0,1) | $0.03706 \pm 0.00018$ | 0.0394 |
| Y(1,1) | $-(4.0 \pm 1.6) \times 10^{-5}$ | ... |
| Y(0,2) | $-7.2 \times 10^{-8}$ (fixed in fit) | ... |

[a]Korek *et al.*'s[106] ground state well depth is ~300 $cm^{-1}$ larger than the experimental ground state well depth of Ref. 12. Since the $T_e$ values reported in Ref. 106 are based on energies relative to the bottom of this theoretical ground state potential, while our experimental $5^3\Pi_0$ potential is referenced to the bottom of the experimental ground state potential of Ref. 12, we have reduced the $T_e$ value of Ref. 106 from the reported value of 24 880 $cm^{-1}$ to make comparison of the theoretical and experimental $5^3\Pi_0$ potentials more meaningful. In effect, this means that the theoretical curves have been shifted such that the ground state asymptotes of the theoretical and experimental potentials coincide.

brational state. Thus the Dunham fit is unlikely to provide an adequate representation of the level energies.

The Dunham coefficients were used to calculate a $5^3\Pi_0$ Rydberg–Klein-Rees (RKR) potential energy curve using Le Roy's computer program RKR1.[105] The calculated turning points are listed in Table 3 of the supplementary materials.[99] The minimum energy of the RKR potential is 66.19 $cm^{-1}$ lower than the minimum of the theoretical NaCs $5^3\Pi_0$ potential of Korek *et al.*[106] (see footnote to Table I), and the equilibrium position of the RKR curve is 0.15 Å greater than the value calculated by those authors. The RMS deviation of the $5^3\Pi_0(v, J)$ level energies calculated from the RKR potential and those measured experimentally is 1.45 $cm^{-1}$. The RKR potential was used as a starting point to apply the IPA method, and this analysis is described in Sec. III B.

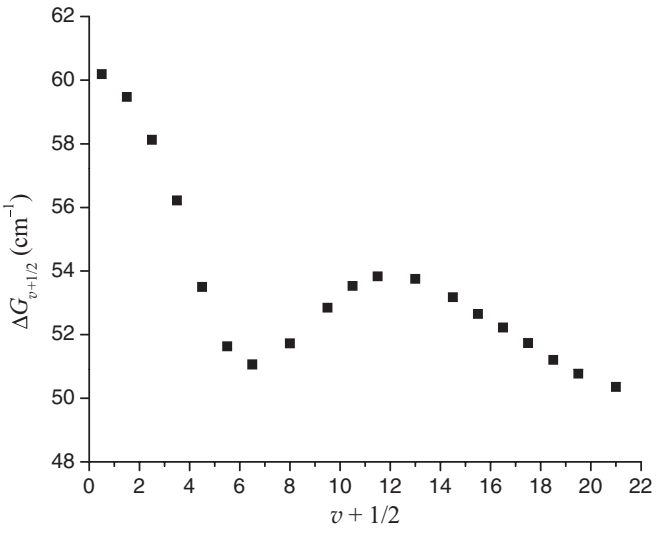


FIG. 6. Measured vibrational level spacings $\Delta G_{v+1/2} = G(v + 1) - G(v)$ for the NaCs $5^3\Pi_0$ state.

## B. The NaCs $5^3\Pi_0$ IPA potential

The IPA method[51] is an iterative approach that tries to find the best potential $V(R)$, such that the calculated ro-vibrational level energies $E_{calc}(v, J)$ agree with the measured energies in the least squares sense. The procedure begins with a reference potential $V_0(R)$ whose energies agree roughly with the experimental values. The program then determines a correction $\delta V(R)$ to the reference potential such that when the Schrödinger equation is solved by applying perturbation theory to the modified potential $V(R) = V_0(R) + \delta V(R)$, the calculated energies match the measured energies in a least squares sense. $V(R)$ then serves as the new reference potential, and the procedure is iterated. During each iteration, $\delta V(R)$ is evaluated at a user defined set of $P$ equidistant points, $R_1$, ... $R_P$, and intermediate values are determined using cubic spline.

In the IPA fitting procedure employed here, we use a modified version[38] of the publicly available IPA program written by Pashov *et al.*[51] We simplified the input files and use subroutines from the program LEVEL to calculate the ro-vibrational level energies for each iteration of the potential. Based on what we learned from the Dunham and RKR fits, one additional level energy $[(v, J) = (3, 61)]$ was also dropped from the IPA fit. Details of the iteration procedure, number of grid points used in each iteration, etc., can be found in Ref. 104.

The final IPA potential is presented in Fig. 7 and compared with the theoretical potential of Korek *et al.*[106] The agreement is quite good. The residual differences between the measured level energies and those calculated using LEVEL with the final IPA potential are presented in Fig. 8. The RMS deviation is 0.029 $cm^{-1}$. The final IPA potential was also able to match the energies of the levels $(v, J) = (5, 29)$, (10, 11), (16, 21), and (16, 25), which weren't used in the fit. Figure 8 includes all $0 \le v \le 22$ energy levels used in the fit as well as those that were excluded due to uncertainty in the assignment of quantum numbers or due to local perturbations. The IPA potential energy curve vs. internuclear separation is given in Table II.

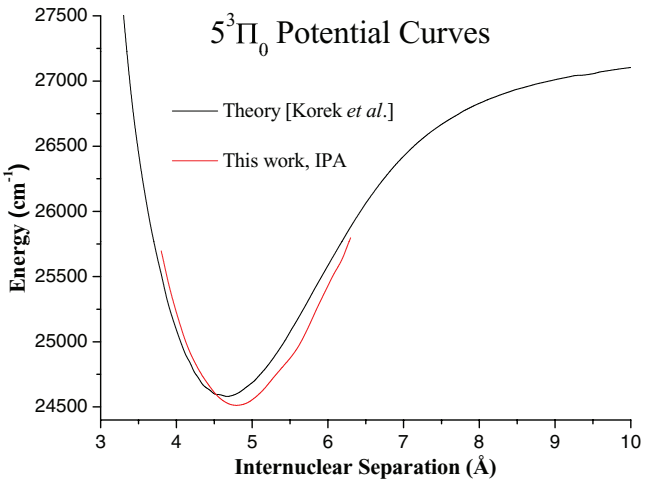


FIG. 7. IPA and theoretical NaCs $5^3\Pi_0$ potential energy curves.

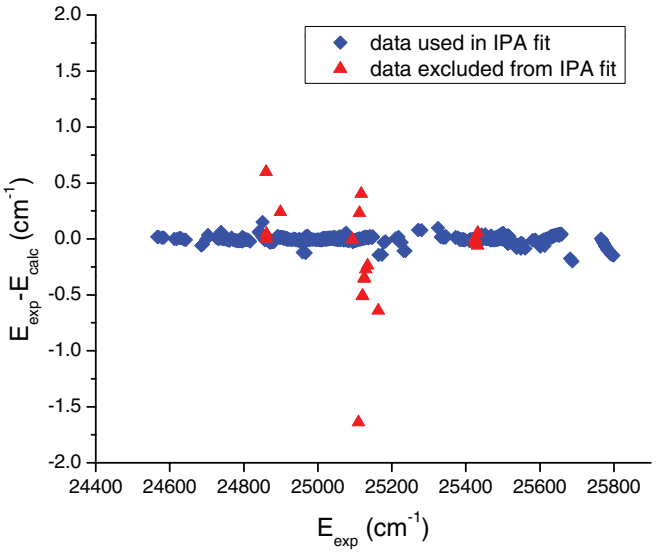


FIG. 8. Differences between experimental NaCs $5^3\Pi_0$ ro-vibrational level energies and those calculated using the program LEVEL 8.0[115] with the present $5^3\Pi_0$ IPA potential. Note that this plot includes all measured levels used in the Dunham coefficient and IPA potential fits (blue diamonds), as well as those that were excluded from the fits (red triangles).

The IPA potential energy curve shows some gentle wiggles on its outer wall. These wiggles appear to be necessary in order for the resulting potential to accurately reproduce the measured ro-vibrational level energies. Indeed, these oscillations are apparent in the vibrational level spacings $\Delta G_{v+1/2} = G(v+1) - G(v)$, which are shown in Fig. 6. Additional iterations and alternative pathways of IPA calculations all led to similar results.

TABLE II. NaCs $5^3\Pi_0$ IPA potential energy curve obtained in this work.

| $R$ (Å) | Energy ($cm^{-1}$) | $R$ (Å) | Energy ($cm^{-1}$) |
|---|---|---|---|
| 3.80 | 25 698.0939 | 5.10 | 24 603.0127 |
| 3.85 | 25 560.9466 | 5.15 | 24 633.1562 |
| 3.90 | 25 436.2403 | 5.20 | 24 666.8511 |
| 3.95 | 25 325.5565 | 5.25 | 24 702.7118 |
| 4.00 | 25 221.3620 | 5.30 | 24 738.0091 |
| 4.05 | 25 126.2943 | 5.35 | 24 771.9514 |
| 4.10 | 25 037.4212 | 5.40 | 24 805.5389 |
| 4.15 | 24 958.1283 | 5.45 | 24 838.2437 |
| 4.20 | 24 889.4402 | 5.50 | 24 873.2577 |
| 4.25 | 24 832.4323 | 5.55 | 24 910.7312 |
| 4.30 | 24 780.2336 | 5.60 | 24 953.2519 |
| 4.35 | 24 732.0151 | 5.65 | 25 003.4153 |
| 4.40 | 24 688.5990 | 5.70 | 25 060.6384 |
| 4.45 | 24 647.4302 | 5.75 | 25 122.3610 |
| 4.50 | 24 610.2410 | 5.80 | 25 186.0408 |
| 4.55 | 24 578.9161 | 5.85 | 25 249.2538 |
| 4.60 | 24 553.2995 | 5.90 | 25 310.5741 |
| 4.65 | 24 534.7244 | 5.95 | 25 370.9411 |
| 4.70 | 24 521.5429 | 6.00 | 25 429.3791 |
| 4.75 | 24 513.8275 | 6.05 | 25 488.5382 |
| 4.80 | 24 511.9027 | 6.10 | 25 543.0925 |
| 4.85 | 24 513.9479 | 6.15 | 25 590.7432 |
| 4.90 | 24 521.8040 | 6.20 | 25 647.1115 |
| 4.95 | 24 535.5707 | 6.25 | 25 723.7552 |
| 5.00 | 24 554.2563 | 6.30 | 25 798.7709 |
| 5.05 | 24 576.6675 | | |

The $5^3\Pi_0$ state must interact strongly with at least one (and probably more than one) nearby electronic state. Such interactions cause global perturbations that slightly shift entire vibrational bands from their unperturbed positions. These interactions cannot be taken into account in the present work because of the current scarcity of data on neighboring states. The IPA potential curve is a single empirical curve that does a good job of reproducing the experimental energies. However, once information on neighboring states becomes available, a coupled-channel approach[40,107,108] will be needed in order to achieve a completely satisfactory analysis.

## IV. THE NaCs $1(a)^3\Sigma^+$ REPULSIVE WALL AND THE $5^3\Pi_0 \rightarrow 1(a)^3\Sigma^+$ RELATIVE TRANSITION DIPOLE MOMENT FUNCTION

The $5^3\Pi_0(v, J) \rightarrow 1(a)^3\Sigma^+$ bound-free continuum fluorescence intensity within a range $d\lambda$ about $\lambda$ is given by[32,37]

$$\frac{dI(\lambda)}{d\lambda}d\lambda = \frac{128\pi^5 c^2 \hbar N_u}{3\lambda^6}\sum_{J'} S(J, J') \times \left[\int_0^\infty \chi_u^{v,J}(R)\mu(R)\chi_\ell^{E_\ell,J'}(R)dR\right]^2 d\lambda, \quad (2)$$

where $N_u$ is the number of molecules in the upper state and $S(J, J')$ is the Hönl–London factor. $\chi_u^{v,J}(R)$ and $\chi_\ell^{E_\ell,J'}(R)$, respectively, are the wave functions for the upper, bound state of energy $E_u$ and for the lower, continuum state of energy $E_\ell$. These wave functions are taken to be real, and $\chi_\ell^{E_\ell,J'}(R)$ is energy normalized. $\mu(R)$ is the transition dipole moment function, and $E_u - E_\ell = hc/\lambda$.

We used a version of Le Roy's BCONT program[109] that was modified by us as described in Ref. 45 to fit the $1(a)^3\Sigma^+$ repulsive wall and $5^3\Pi_0 \rightarrow 1(a)^3\Sigma^+$ relative transition dipole moment function to the resolved NaCs $5^3\Pi_0(v, J) \rightarrow 1(a)^3\Sigma^+$ bound-free fluorescence spectra. BCONT allows the user to input upper and lower state potentials, as well as the transition dipole moment function for the transition coupling the two states, and simulates bound-free fluorescence spectra from particular user-selected ro-vibrational levels of the upper state to the continuum of lower state levels according to Eq. (2). The modified version of BCONT also allows us to simulate unresolved bound-bound contributions to the oscillatory continua and includes a convolution algorithm to take the finite monochromator resolution into account. The program considers multiple experimental spectra and carries out a global least squares fit of the simulated spectra to the experimental spectra in order to determine the lower state repulsive wall and transition dipole moment function.

The shallow bound region of the $1(a)^3\Sigma^+$ state has been mapped experimentally by Docenko *et al.*,[12,49] who measured more than 3000 transition frequencies to about 940 bound ro-vibrational levels of the $1(a)^3\Sigma^+$ state using a Bruker Fourier-transform spectrometer (FTS). Due to the large size of their data set, and the superior resolution of the Bruker FTS com-

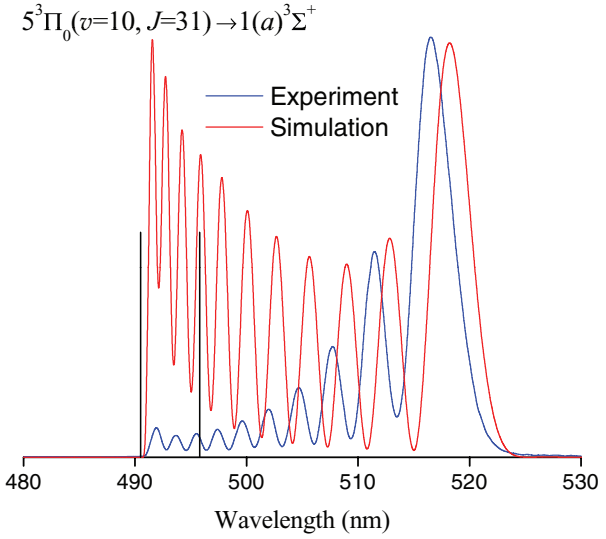


FIG. 9. NaCs $5^3\Pi_0(v = 10, J = 31) \rightarrow 1(a)^3\Sigma^+$ bound-free spectrum and simulation using the present IPA $5^3\Pi_0$ potential and the Docenko *et al.*[12] $1(a)^3\Sigma^+$ potential (including the $V_{\text{Wall}}(R) \sim R^{-3}$ repulsive wall). In the simulation, the transition dipole moment function was taken to be constant with $R$. The pair of vertical black solid lines represents the range of wavelengths in which bound–bound transitions occur.

pared to our monochromator, we held the bound portion of the $1(a)^3\Sigma^+$ potential fixed in our fitting, and only allowed the repulsive wall to vary. The IPA $5^3\Pi_0$ potential was used as the upper state in all simulations.

BCONT simulates the bound-free fluorescence as a function of vacuum wavelength while the monochromator records as a function of wavelength in air. Thus the wavelength scale of each experimental spectrum was converted to vacuum wavelength before the fitting was carried out. All bound-free spectra shown in Figs. 3, 9, and 12 are plotted vs. vacuum wavelength.

The classical Franck-Condon approximation (CFCA) states that electronic transitions are instantaneous, and therefore both internuclear separation and kinetic energy should be preserved during a transition. In a case like the one considered here, where the difference potential, $V_{5^3\Pi_0}(R) - V_{1(a)^3\Sigma^+}(R)$, is monotonic, each internuclear separation can be associated with a unique bound-free emission wavelength. Although the CFCA is only an approximation, it provides a good starting point for the fit since it implies that the locations of the peaks and troughs of the oscillatory bound-free spectra are determined primarily by the shapes of the upper and lower state potentials, while the peak amplitudes depend primarily on the transition dipole moment function, $\mu(R)$.

We started with the IPA $5^3\Pi_0$ potential determined above and the $1(a)^3\Sigma^+$ potential reported by Docenko *et al.*[12] The $1(a)^3\Sigma^+$ potential well region was determined by Docenko *et al.* using very extensive bound–bound transition data. Onto this well, they attached a simple repulsive wall extrapolated as $V_{\text{Wall}}(R) \sim R^{-3}$, which provided a useful starting point for us. The full IPA $5^3\Pi_0$ potential and the Docenko $1(a)^3\Sigma^+$ well region were fixed in our fits, but the $1(a)^3\Sigma^+$ repulsive wall was allowed to vary. The repulsive wall was constrained to join smoothly and continuously to the bound $1(a)^3\Sigma^+$ state well.

Using the IPA $5^3\Pi_0$ potential determined above, the Docenko *et al.* $1(a)^3\Sigma^+$ potential (including the $V_{\text{Wall}}(R) \sim R^{-3}$ repulsive wall), and a constant (with $R$) transition dipole moment function, we simulated the NaCs $5^3\Pi_0(v = 10, J = 31) \rightarrow 1(a)^3\Sigma^+$ bound-free spectrum shown in Fig. 9. The lack of agreement between the simulated and experimental positions of the peaks on the long wavelength end of the band was a clear indication that adjustments were needed to the $1(a)^3\Sigma^+$ repulsive wall. In addition, the fact that the simulated peak amplitudes were much too large at short wavelength implied that the transition dipole moment must fall with increasing $R$. Using a manual fit to the data, reasonable agreement in peak positions and amplitudes was found using the $1(a)^3\Sigma^+$ repulsive wall and transition dipole moment functions shown in Figs. 6.3 and 6.6 of Ref. 104, respectively. These were used to provide a starting point for the global fit described below.

The modified version of BCONT[45,109] accepts as input the wavelength and intensity corrected bound-free spectra, and the user selects the functional forms of the repulsive wall and transition dipole moment from short menus of possible choices. The $5^3\Pi_0$ IPA potential and the bound portion of the $1(a)^3\Sigma^+$ potential (i.e., the region $R > 4.78$ Å) were included in the BCONT input file, and they were not allowed to vary (the current version of the program doesn't have the capability to modify the upper state potential). In the fit we included $5^3\Pi_0(v, J) \rightarrow 1(a)^3\Sigma^+$ spectra for $(v, J) = (0, 31)$, (1, 25), (3, 31), (5, 23), (6, 43), (9, 33), (10, 31), (12, 33), (14, 31), (15, 33), (17, 24), (18, 31), (19, 43), and (22, 43), which provide good coverage over the full range $v = 0$–22. Each of these was also a relatively clean spectrum in which changes in the total green fluorescence intensity due to laser frequency drift and other undesirable effects were minimal.

The Docenko *et al.* $1(a)^3\Sigma^+$ potential was read in for points in the range 4.78 Å $< R <$ 27.57 Å on a grid spacing of 0.01 Å. BCONT interpolates between these points to create a smooth potential and extrapolates to larger $R$, asymptotically approaching the separated atom energy of $E_{\text{Na}(3S)+\text{Cs}(6S)} = 4954.237\ \text{cm}^{-1}$ measured from the bottom of the $1(X)^1\Sigma^+$ potential.[12] We chose to use a $1(a)^3\Sigma^+$ potential repulsive wall of the form

$$V_{\text{Wall}}(R) = X_1 + X_2 \exp\left[-(R - R_0)\sum_{n=0}^{N_P} A_n z^n\right], \qquad (3)$$

where $X_1$ and $X_2$ are determined by a fit of the two innermost read-in points, $R$ is the internuclear separation, $R_0$ is a user selected value, and the expansion coordinate is $z = \frac{R-R_0}{R_0}$. The form of the transition dipole moment function is also defined by the user. Our modified version of the program allows use of a switching function[45] to combine two different functional forms to describe the $\mu(R)$ function; one at small $R$ and one at large $R$. The width and location (in $R$) of the switching point are controlled by the user and can be allowed to vary in fits. Here we chose to use an $R^n$ power series to describe the transition dipole moment on the small $R$ side, and a $\frac{1}{R^{2n}}$ power series for large $R$ where the transition dipole moment seems to approach zero. This is consistent with the fact that the $5^3\Pi_0$ state dissociates to the $\text{Na}(3S_{1/2}) + \text{Cs}(6D_{5/2})$ separated atom limit,[110] while the $1(a)^3\Sigma^+$ state dissociates to

Na(3*S*) + Cs(6*S*), and such a transition is highly unlikely in the asymptotic region. The functional form of the transition dipole moment was thus chosen to be

$$\mu(R) = \left[\sum_{n=0}^{N_\alpha} \alpha_n R^n\right] S\left(\frac{R - R_x}{w}\right) + \left[\sum_{n=1}^{N_\beta} \beta_n \left(\frac{1}{R^2}\right)^n\right] \times \left[1 - S\left(\frac{R - R_x}{w}\right)\right], \quad (4)$$

where the switching function $S(y)$ is defined by

$$S(y) = \begin{cases} 1 - \frac{1}{2}\exp\left[-\left(y - \frac{1}{\sqrt{2}}\right)^2 + \frac{1}{2}\right] & \text{if } y < 0 \\ \frac{1}{2}\exp\left[-\left(y + \frac{1}{\sqrt{2}}\right)^2 + \frac{1}{2}\right] & \text{if } y \geq 0 \end{cases}, \quad (5)$$

with the argument $y = \frac{R - R_x}{w}$ so that $R_x$ is the switching point and $w$ is related to the width of the region in which the switch occurs (see Ref. 45).

We found that varying all parameters simultaneously in one fit required too much computer time. Therefore, we started by varying just one parameter in either the repulsive wall or transition dipole moment function while fixing the rest of the parameters at their best known values. This allowed a fit to finish in a reasonable amount of time (a few minutes to about an hour). The new parameter value was then used in the initial guess for the next iteration where another parameter was also allowed to vary in addition to the first one. In this way, we built up the number of parameters until the fit included $A_0$, $A_1$, and $A_2$ terms (see Eq. (3)), $\alpha_0$ (fixed to the value 1), $\alpha_1$, $\alpha_2$, $\beta_1$, $\beta_2$, and $\beta_3$ terms (see Eq. (4)), and the switching function position $R_x$ (see Eqs. (4) and (5)). The exclusion of a $\beta_0$ term ensures that the transition dipole moment function goes to zero at large $R$, and we fixed $\alpha_0 = 1$ to set the overall scale. An individual scaling factor for each simulation was determined at the end to maximize its agreement with the corresponding experimental spectrum. The measured bound-free emission intensities are in arbitrary units (depending on pump and probe transitions, laser intensities, beam overlap, etc.), so we can only extract the *relative* transition dipole moment from our data. The switching function width, $w$, in Eq. (4) was fixed at the value 0.50 Å for all fits because it tended to become unphysically small if allowed to vary, causing the transition dipole moment function to contain sharp features near the switching region. This was the same value used in our fitting of the NaK $4^3\Sigma^+ \rightarrow 1(a)^3\Sigma^+$ transition dipole moment.[45] In the final iteration, we allowed all nine adjustable parameters ($A_0$, $A_1$, $A_2$, $\alpha_1$, $\alpha_2$, $\beta_1$, $\beta_2$, $\beta_3$, and $R_x$) to vary simultaneously. Table III lists the final set of parameters and indicates which were allowed to vary in the fit. Figures 10 and 11, respectively, show the NaCs $1(a)^3\Sigma^+$ repulsive wall and the NaCs $5^3\Pi_0 \rightarrow 1(a)^3\Sigma^+$ relative transition dipole moment function determined in this work.

Comparisons of the NaCs $5^3\Pi_0(v, J) \rightarrow 1(a)^3\Sigma^+$ experimental spectra with simulations based on the parameters determined in the global fit are shown in Fig. 12. As can be seen, the agreement between the simulations and the experimental spectra is reasonable, but far from perfect.

TABLE III. Parameters describing the NaCs $1(a)^3\Sigma^+$ repulsive wall [Eq. (3)] and the $5^3\Pi_0 \rightarrow 1(a)^3\Sigma^+$ transition dipole moment function [Eqs. (4) and (5)] resulting from the global fit of the $5^3\Pi_0(v, J) \rightarrow 1(a)^3\Sigma^+$ resolved bound-free fluorescence spectra.

| Parameter | Vary in fit? | Final fitted value |
|---|---|---|
| $R_0$ | No | 4.7800 Å |
| $X_1$ | Fit from bound region | 4574.1906 $cm^{-1}$ |
| $X_2$ | Fit from bound region | 371.0195 $cm^{-1}$ |
| $A_0$ | Yes | 2.0675 $Å^{-1}$ |
| $A_1$ | Yes | 3.8009 $Å^{-1}$ |
| $A_2$ | Yes | 12.0204 $Å^{-1}$ |
| $\alpha_0$ | No | 1.00 Debye |
| $\alpha_1$ | Yes | $-7.004 \times 10^{-1}$ Debye-$Å^{-1}$ |
| $\alpha_2$ | Yes | $8.6925 \times 10^{-2}$ Debye-$Å^{-2}$ |
| $\beta_0$ | No | 0.00 Debye |
| $\beta_1$ | Yes | 75.4458 Debye-$Å^2$ |
| $\beta_2$ | Yes | $-5.8124 \times 10^3$ Debye-$Å^4$ |
| $\beta_3$ | Yes | $1.0703 \times 10^5$ Debye-$Å^6$ |
| $R_x$ | Yes | 5.4510 Å |
| $w$ | No | 0.50 Å |

The reduced $\chi^2$ value is given by

$$\chi^2 = \frac{1}{N - m}\sum_{i=0}^{N}\left(\frac{I_i^{\text{Obs}} - I_i^{\text{Calc}}}{\sigma}\right)^2, \quad (6)$$

where $I_i^{\text{Obs}}$ and $I_i^{\text{Calc}}$ are the observed and calculated intensities, respectively, $N$ is the number of data points, $m$ is the number of adjustable parameters, and $\sigma$ is the error bar on each measurement. The value of $\chi^2$ for the final iteration of the global fit described above is 42.7. This is a very large value, especially considering that by eye, the simulations do a reasonable job of reproducing the overall relative intensities of the peaks in the experimental spectra. However, a large

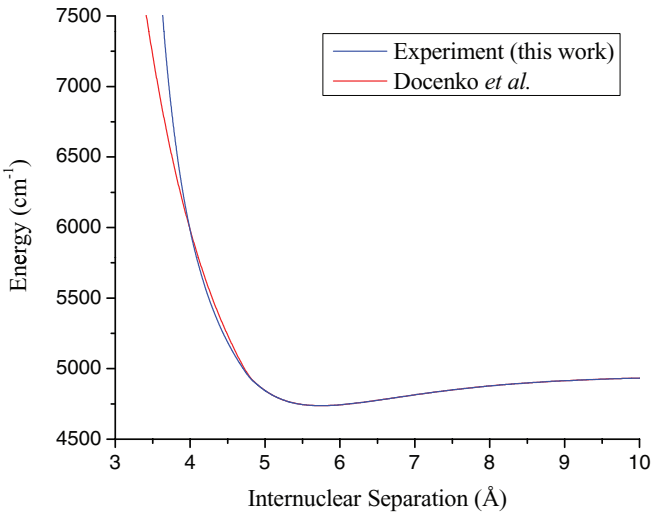


FIG. 10. Best "global fit" of the NaCs $1(a)^3\Sigma^+$ state repulsive wall. The repulsive wall obtained in the global fit presented in this work is plotted along with the $1(a)^3\Sigma^+$ potential of Docenko *et al.*[12] (including their $R^{-3}$ extrapolation of the repulsive wall).

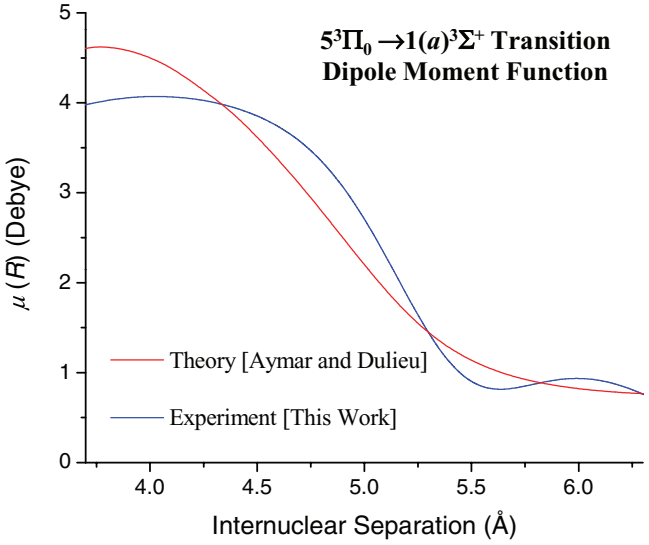


FIG. 11. NaCs $5^3\Pi_0 \rightarrow 1(a)^3\Sigma^+$ transition dipole moment function. The blue curve represents the best "global fit" of the $5^3\Pi_0 \rightarrow 1(a)^3\Sigma^+$ relative transition dipole moment function from the present work, while the red curve is the theoretical $5^3\Pi_0 \rightarrow 1(a)^3\Sigma^+$ transition dipole moment function of Aymar and Dulieu.[111] Since the experimental curve is only a relative transition dipole moment function, it has been normalized (by multiplying the function described by Eqs. (4) and (5) and the parameters listed in Table III by the factor −9.9066) to the theoretical curve in a least squares sense over the range 3.7 Å $< R <$ 6.3 Å.

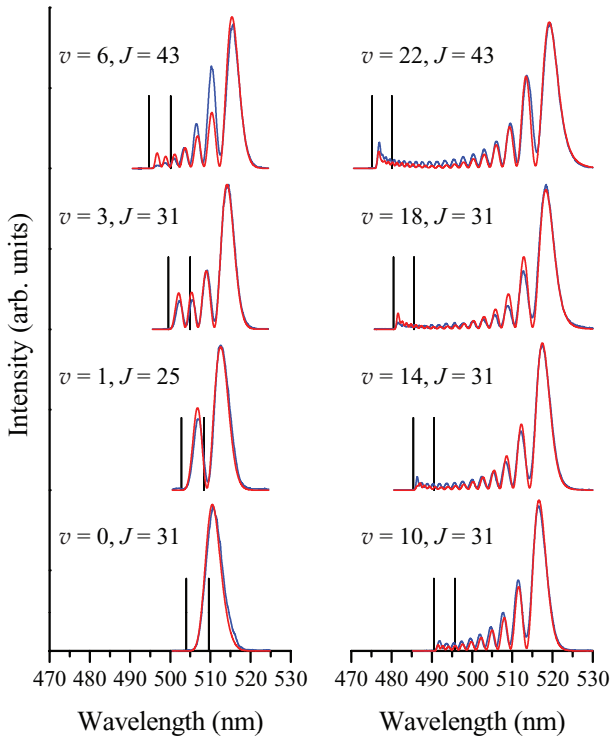


FIG. 12. NaCs $5^3\Pi_0(v, J) \rightarrow 1(a)^3\Sigma^+$ resolved fluorescence spectra (blue) and simulated spectra (red) based on the $1(a)^3\Sigma^+$ state repulsive wall and $5^3\Pi_0 \rightarrow 1(a)^3\Sigma^+$ relative transition dipole moment function global fit parameters. Comparisons of experimental and simulated resolved fluorescence spectra from additional upper levels can be found in Ref. 104. Each pair of vertical black solid lines represents the range of wavelengths in which bound–bound transitions occur.

reduced $\chi^2$ value indicates that, on average, the simulation fails to reproduce the experimental spectra within the error bars. We believe that the error bars used in the fits are accurate (the experimental spectra have excellent signal-to-noise ratios); they are based on the peak-to-peak magnitude of the noise observed in the recorded spectra. However, the fact that our global fit is unable to reproduce the experimental spectra within the error bars suggests that either our model is not sufficiently flexible, or that the accuracy of the $5^3\Pi_0$ potential or transition dipole moment function is not sufficient. We believe that the $5^3\Pi_0$ potential determined by the IPA analysis provides the best single-potential model currently available to represent the measured level energies. But the $5^3\Pi_0$ state experiences global perturbations due to one or more nearby, and as yet unmapped, electronic states; once these are determined experimentally, a coupled-channel analysis may lead to a more accurate description.

Figure 11 compares the theoretical NaCs $5^3\Pi_0 \rightarrow 1(a)^3\Sigma^+$ transition dipole moment function of Aymar and Dulieu[111] with the experimental transition dipole moment function determined in the present work. Since we only determine a relative transition dipole moment function in the experiment, the experimental curve in Fig. 11 has been normalized to the theoretical curve in a least squares sense over the range 3.7 Å $< R <$ 6.3 Å. As can be seen, the agreement between theory and experiment is quite good, especially considering perturbations that are likely to affect the upper $5^3\Pi_0(v, J)$ levels of the experimental spectra, the uncertainties in the fitting of the $5^3\Pi_0$ potential and $5^3\Pi_0 \rightarrow 1(a)^3\Sigma^+$ transition dipole moment function, and the fact that the theoretical calculations do not consider fine structure.

## V. HYPERFINE STRUCTURE

Hyperfine structure has been observed for many triplet electronic states of alkali diatomic molecules. In those cases where there is an appreciable amount of atomic $s$ state orbital in the electron wave function (i.e., states built on the $M_2^+(X^2\Sigma^+)$ ion-core ground state including most states lying below the first doubly excited asymptote), it has been found that the Fermi contact term is the dominant hyperfine interaction.[36,82,90,92,112] (For example, the nuclear-spin–electron-orbital and non-contact electron-spin–nuclear-spin dipolar interaction terms were found to be ∼30 times smaller than the Fermi contact term in the $Na_2$ $2^3\Pi_g$ state;[85] one of the few cases where such terms have been determined. In general, the nuclear-spin–electron-orbital and electron-spin–nuclear-spin dipolar interaction terms don't produce splittings that are large enough to resolve. The electric quadrupole interaction is expected to have an even smaller effect.) When the Fermi contact term is dominant, the splittings are found to be proportional to the atomic Fermi contact constant; i.e., the molecular Fermi constant is $b_F \approx b_F^{\text{atomic}}/4$ for homonuclear molecules[80,85,90] and $b_F \approx b_F^{\text{atomic}}/2$ for heteronuclear molecules[39] (for a heteronuclear molecule $b_F^{\text{atomic}}$ is the larger of the two atomic Fermi contact constants). In particular, clearly resolved hyperfine structure has been observed for levels of the NaK $1(b)^3\Pi_0$, $3^3\Pi_0$, and $4^3\Pi_0$ states. Therefore, it

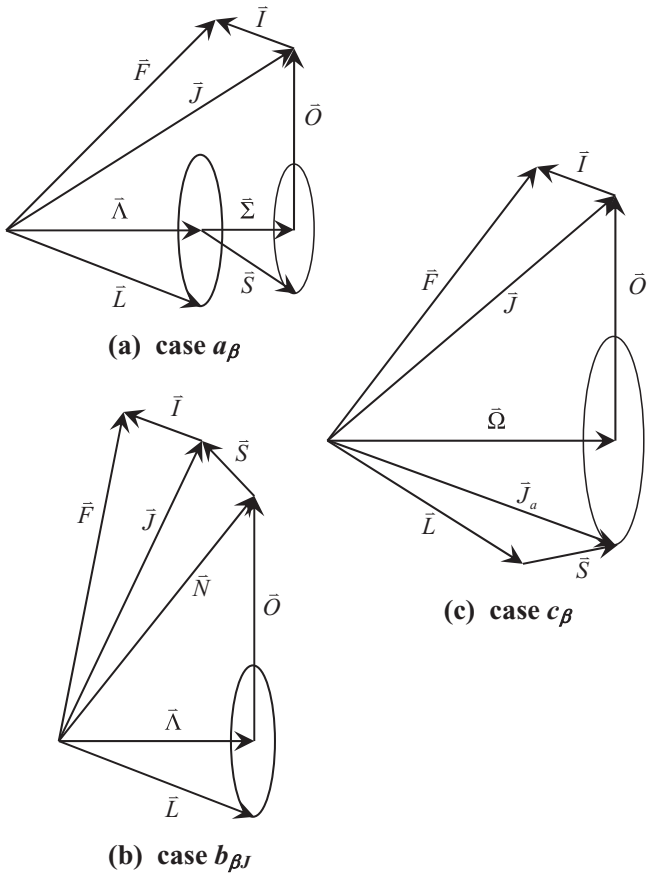


FIG. 13. Vector coupling diagrams used to determine hyperfine structure in the case $a_\beta$, $b_{\beta J}$, and $c_\beta$ limits.

is a bit surprising that the $5^3\Pi_0(v, J)$ levels of NaCs show no observable hyperfine structure under our resolution, despite the very large atomic cesium Fermi constant.[113] However, we believe this can be explained by invoking a simple vector coupling model for the hyperfine structure.[114]

In the lighter alkali molecules and for typical $J$ values found in thermal vapors, most electronic states can be described by Hund's case $b$, and the hyperfine coupling scheme can be described by coupling cases $b_{\beta J}$ or $b_{\beta S}$. Figure 13 shows vector coupling diagrams for Hund's coupling cases $a_\beta$, $b_{\beta J}$, and $c_\beta$ (see also Fig. 8-1 in Ref. 112). In these diagrams, $\vec{L}$ is the total electron orbital angular momentum, $\vec{S}$ is the total electron spin, and $\vec{\Lambda}$ and $\vec{\Sigma}$ are the components of $\vec{L}$ and $\vec{S}$, respectively, along the internuclear axis. $\vec{O}$ is the nuclear orbital angular momentum (nuclear rotation) vector and $\vec{I}$ is the nuclear spin vector. The Fermi contact hyperfine term in the Hamiltonian is $E_{\rm hfs} = b_F \vec{I} \cdot \vec{S}$.

Except for $^3\Sigma$ states, most triplet electronic states of the lighter alkali molecules follow coupling case $b_{\beta J}$. A vector coupling model for this case was described in Ref. 36 and is summarized here. Since $\vec{S}$ interacts more strongly with $\vec{N}$ than with $\vec{I}$ (as shown in Fig. 13(b)), $\vec{S}$ and $\vec{N}$ precess around their resultant $\vec{J} = \vec{S} + \vec{N}$. Then one can approximate the hyperfine interaction using $\vec{S}_J$ which is parallel to $\vec{J}$ and is the average value of $\vec{S}$,

$$E_{\rm hfs} = b_F \vec{I} \cdot \vec{S} \approx b_F \vec{I} \cdot \vec{S}_J = b_F \vec{I} \cdot \vec{J} \frac{|\vec{S}_J|}{|\vec{J}|}. \tag{7}$$

The hyperfine energies for the three fine-structure components of a triplet state ($J = N - 1$, $N$, $N + 1$) can be evaluated using geometrical considerations to determine the projection of $\vec{S}$ onto $\vec{J}$. The results have been given in Ref. 112 (see also Ref. 36),

$$\begin{aligned} E_{\rm hfs}^{J=N-1} &= -\frac{b_F}{2(J+1)}[F(F+1) - I(I+1) - J(J+1)]\hbar^2, \\ E_{\rm hfs}^{J=N} &= \frac{b_F}{2J(J+1)}[F(F+1) - I(I+1) - J(J+1)]\hbar^2, \\ E_{\rm hfs}^{J=N+1} &= \frac{b_F}{2J}[F(F+1) - I(I+1) - J(J+1)]\hbar^2. \end{aligned} \tag{8}$$

The hyperfine energies for each value of $J$ follow a Landé rule. For each possible $J$, the hyperfine splittings $\Delta E_{\rm hfs}^J = E_{\rm hfs}^J(F) - E_{\rm hfs}^J(F-1)$ are

$$\begin{aligned} \Delta E_{\rm hfs}^{J=N-1} &= -b_F \hbar^2 \frac{F}{(J+1)}, \\ \Delta E_{\rm hfs}^{J=N} &= b_F \hbar^2 \frac{F}{J(J+1)}, \\ \Delta E_{\rm hfs}^{J=N+1} &= b_F \hbar^2 \frac{F}{J}. \end{aligned} \tag{9}$$

The splittings of the $J = N$ component are much smaller than those of the $J = N \pm 1$ components for typical values of $J$ ($\sim$30) in thermal alkali vapors. This difference is due to the fact that for $J = N$, $\vec{S}$ is almost perpendicular to $\vec{J}$ so that $|\vec{S}_J|$ is very small. In contrast, for the $J = N \pm 1$ components, the splitting is on the order of $b_F$ in appropriate units. Splittings of this same order are also observed in case $b_{\beta S}$, although the line structure is quite different.

Heavier alkali molecules generally have larger spin-orbit interactions, and we expect electronic states with $L \neq 0$, $\Lambda \neq 0$ to follow Hund's case $a$ or case $c$. Due to the presence of the heavy Cs atom, we expect NaCs to follow coupling case $a_\beta$ or $c_\beta$, where the subscript $\beta$ indicates that the nuclear spin $\vec{I}$ is not coupled to the internuclear axis, but rather to $\vec{J}$ ($\vec{F} = \vec{I} + \vec{J}$).

In coupling case $a$, the electron orbital angular momentum $\vec{L}$ and the electron spin $\vec{S}$ both couple strongly to the internuclear axis, and only their components $\vec{\Lambda}$ and $\vec{\Sigma}$ are relevant (see Fig. 13(a)). $\vec{\Lambda} + \vec{\Sigma} = \vec{\Omega}$. $\vec{\Omega}$ couples with the nuclear rotation $\vec{O}$ to form $\vec{J}$ ($\vec{J} = \vec{O} + \vec{\Omega} = \vec{O} + \vec{\Lambda} + \vec{\Sigma}$). Thus in case $a_\beta$ only the components of $\vec{O}$, $\vec{\Lambda}$, and $\vec{\Sigma}$ along $\vec{J}$ survive the averaging. The Fermi contact hyperfine interaction in the $a_\beta$ limit is given by

$$E_{\rm hfs} = b_F \vec{I} \cdot \vec{S} \approx b_F \vec{I} \cdot \vec{J} \frac{|\vec{\Sigma}_J|}{|\vec{J}|}. \tag{10}$$

From geometry it can be shown that[104]

$$\frac{|\vec{\Sigma}_J|}{|\vec{J}|} = \frac{\Sigma}{\Omega}\frac{|\vec{\Omega}_J|}{|\vec{J}|} = \frac{\Sigma|\vec{\Omega}|^2}{\Omega|\vec{J}|^2} = \frac{\Sigma\Omega}{J(J+1)}, \tag{11}$$

so that the Fermi contact hyperfine interaction can be expressed as

$$E_{\rm hfs} = b_F \vec{I}\cdot\vec{S} \approx \frac{b_F\Sigma\Omega}{2J(J+1)} \times [F(F+1) - I(I+1) - J(J+1)]\hbar^2, \tag{12}$$

and hyperfine splittings are given by

$$\Delta E^J_{\rm hfs} = E^J_{\rm hfs}(F) - E^J_{\rm hfs}(F-1) = b_F\hbar^2\frac{\Sigma\Omega F}{J(J+1)}. \tag{13}$$

Note that the hyperfine splitting is zero in this limit if $\Sigma = 0$ (i.e., for a $^3\Pi_1$ or $^3\Delta_2$ component), or if $\Omega = 0$ (i.e., for a $^3\Pi_0$ component). The splitting will increase for an $\Omega = 0$ component with increasing $J$ as the coupling scheme moves away from the case $a$ limit and approaches the case $b$ limit. However, even when $\Sigma$ and $\Omega$ are not zero, they are still typically small numbers (of order $\sim$1), so that the case $a_\beta$ hyperfine splittings are smaller than the case $b_{\beta J}$ $J = N \pm 1$ component splittings by a factor of order $J$.

In Hund's case $c$, $\vec{L}$ and $\vec{S}$ couple most strongly to each other to form the intermediate vector $\vec{J}_a$, which then precesses rapidly around the internuclear axis such that only its component along the axis, $\vec{\Omega}$, is relevant (see Fig. 13(c)). Again, $\vec{J} = \vec{O} + \vec{\Omega}$. Thus in hyperfine case $c_\beta$ there is one more level of averaging of the electron spin vector $\vec{S}$ before it couples to $\vec{I}$,

$$E_{\rm hfs} = b_F\vec{I}\cdot\vec{S} \approx b_F\vec{I}\cdot\vec{J}_a\frac{|\vec{S}_{J_a}|}{|\vec{J}_a|} \approx b_F\vec{I}\cdot\vec{\Omega}\frac{|\vec{S}_{J_a}|}{|\vec{J}_a|} \approx b_F\vec{I}\cdot\vec{\Omega}_J\frac{|\vec{S}_{J_a}|}{|\vec{J}_a|} \approx b_F\vec{I}\cdot\vec{J}\frac{|\vec{\Omega}_J|}{|\vec{J}|}\frac{|\vec{S}_{J_a}|}{|\vec{J}_a|}. \tag{14}$$

In the case $a_\beta$ analysis, it was shown that $|\vec{\Omega}_J|/|\vec{J}| = |\vec{\Omega}|^2/|\vec{J}|^2 = \Omega^2/J(J+1)$.[104] $|\vec{S}_{J_a}|/|\vec{J}_a|$ can be evaluated geometrically in terms of $|\vec{J}_a|^2$, $|\vec{L}|^2$, and $|\vec{S}|^2$ with expectation values $|\vec{J}_a|^2 = J_a(J_a+1)\hbar^2$, $|\vec{L}|^2 = L(L+1)\hbar^2$, and $|\vec{S}|^2 = S(S+1)\hbar^2$.[104] Although $J_a$ and $L$ are not good quantum numbers, we can write approximately[104]

$$b_F\vec{I}\cdot\vec{S} \approx b_F\vec{I}\cdot\vec{J}\frac{\Omega^2}{J(J+1)}\frac{J_a(J_a+1) + S(S+1) - L(L+1)}{2J_a(J_a+1)} = \frac{b_F}{2}\hbar^2[F(F+1) - I(I+1) - J(J+1)]\frac{\Omega^2}{J(J+1)} \times \frac{J_a(J_a+1) + S(S+1) - L(L+1)}{2J_a(J_a+1)}. \tag{15}$$

For a triplet state, $S = 1$, $J_a$ takes on three possible values, $J_a = L-1, L, L+1$, and we obtain

$$\begin{aligned} E^{J_a=L-1}_{\rm hfs} &= b_F\vec{I}\cdot\vec{S} \approx -\frac{b_F}{2}\hbar^2[F(F+1) - I(I+1) - J(J+1)]\frac{\Omega^2}{J(J+1)}\frac{1}{(\Omega+1)}, \\ E^{J_a=L}_{\rm hfs} &= b_F\vec{I}\cdot\vec{S} \approx \frac{b_F}{2}\hbar^2[F(F+1) - I(I+1) - J(J+1)]\frac{\Omega}{J(J+1)}\frac{1}{(\Omega+1)}, \\ E^{J_a=L+1}_{\rm hfs} &= b_F\vec{I}\cdot\vec{S} \approx \frac{b_F}{2}\hbar^2[F(F+1) - I(I+1) - J(J+1)]\frac{\Omega}{J(J+1)}, \end{aligned} \tag{16}$$

where in the last step on the right hand side of each equation, we have replaced $J_a$ by its component along the internuclear axis $\Omega$ because $\vec{J}_a$ precesses rapidly about the axis. Finally, the splittings $\Delta E^{J_a,J}_{\rm hfs} = E^{J_a,J}_{\rm hfs}(F) - E^{J_a,J}_{\rm hfs}(F-1)$ are given by

$$\begin{aligned} \Delta E^{J_a=L-1}_{\rm hfs} &\approx -b_F\hbar^2\frac{F}{J(J+1)}\frac{\Omega^2}{(\Omega+1)}, \\ \Delta E^{J_a=L}_{\rm hfs} &\approx b_F\hbar^2\frac{F}{J(J+1)}\frac{\Omega}{(\Omega+1)}, \\ \Delta E^{J_a=L+1}_{\rm hfs} &\approx b_F\hbar^2\frac{F}{J(J+1)}\Omega. \end{aligned} \tag{17}$$

Each of these three expressions yield splittings of 0 for $\Omega = 0$ as in case $a_\beta$. For $\Omega \neq 0$ and small $J$, these splittings are comparable to the atomic splittings. However, for $J$ values typical of thermal temperatures, we have $F \sim J$ while $\Omega \sim 1$. Therefore in this limit, we expect the splittings to be smaller than for the $J = N \pm 1$ components in case $b_{\beta J}$ by a factor on the order of $J$.

Since the NaCs $5^3\Pi_0$ state is expected to follow coupling case $c_\beta$ or $a_\beta$, we see that hyperfine splittings should be of order $b_F/J$ in appropriate units. Thus even though the atomic Cs Fermi contact constant $b_F$ is more than a factor of 2.5 larger than that of either Na or K, for typical $J$ values $J \sim$ 30–60, we expect the NaCs $5^3\Pi_0$ state hyperfine splittings to be approximately an order of magnitude smaller than those observed for the NaK $^3\Pi_0$ states which follow case $b_{\beta J}$. The factors of $\Omega = 0$ in the numerators of Eqs. (13) and (17) mean that, to the extent that the NaCs $5^3\Pi_0$ state is well described by the case $c_\beta$ or $a_\beta$ coupling schemes (e.g., especially

at small $J$), the level hyperfine splittings should be identically zero.

## VI. CONCLUSIONS

In conclusion, we have carried out the first experimental study of the NaCs $5^3\Pi_0$ state using the PFOODR method. In all, we have measured the energies of 401 different $5^3\Pi_0(v, J)$ levels in the range $v = 0$–34. We then used 359 of these levels, in the range $v = 0$–22, to map the $5^3\Pi_0$ electronic potential with the IPA method. The final $5^3\Pi_0$ IPA potential was able to reproduce the fitted level energies with an RMS deviation of 0.029 $cm^{-1}$. We find that the theoretical NaCs $5^3\Pi_0$ potential of Korek *et al.*[106] is in fairly good agreement with the IPA potential determined here (see Fig. 7 and Table I).

Fourteen resolved, oscillating bound-free $5^3\Pi_0(v, J) \rightarrow 1(a)^3\Sigma^+$ continuum emission spectra were compared with simulations, and a global fit of parameters describing the repulsive wall of the $1(a)^3\Sigma^+$ state and the $5^3\Pi_0 \rightarrow 1(a)^3\Sigma^+$ transition dipole moment function was carried out. The overall quality of the fit can be described as only fair. This appears to be due to the fact that we chose not to vary the upper IPA $5^3\Pi_0$ state potential in the global fit. It is clear that the upper $5^3\Pi_0$ state interacts strongly with other electronic states and that a more complete, coupled-channel analysis will be required once more information on neighboring states is available. We have already observed levels of several other electronic states lying in the same energy region, including quite a few levels of a state that we have tentatively identified as $4^3\Pi_0$. Despite the uncertainties, our experimental relative $5^3\Pi_0 \rightarrow 1(a)^3\Sigma^+$ transition dipole moment function $\mu(R)$ is in excellent agreement with the theoretical curve of Aymar and Dulieu,[111] verifying the high quality of those calculations.

## ACKNOWLEDGMENTS

This work was supported by the National Science Foundation (NSF) through Grant Nos. PHY-0652938 and PHY-0968898.

[1] H. Wang and W. C. Stwalley, J. Chem. Phys. **108**, 5767 (1998).
[2] J. P. Shaffer, W. Chalupczak, and N. P. Bigelow, Phys. Rev. A **60**, R3365 (1999).
[3] F. Masnou-Seeuws and P. Pillet, Adv. At. Mol. Opt. Phys. **47**, 53 (2001).
[4] D. Wang, J. Qi, M. F. Stone, O. Nikolayeva, H. Wang, B. Hattaway, S. D. Gensemer, P. L. Gould, E. E. Eyler, and W. C. Stwalley, Phys. Rev. Lett. **93**, 243005 (2004).
[5] M. W. Mancini, G. D. Telles, A. R. L. Caires, V. S. Bagnato, and L. G. Marcassa, Phys. Rev. Lett. **92**, 133203 (2004).
[6] S. Kotochigova, E. Tiesinga, and P. Julienne, Eur. Phys. J. D **31**, 189 (2004).
[7] S. Azizi, M. Aymar, and O. Dulieu, Eur. Phys. J. D **31**, 195 (2004).
[8] C. Haimberger, J. Kleinert, M. Bhattacharya, and N. P. Bigelow, Phys. Rev. A **70**, 021402(R) (2004).
[9] A. J. Kerman, J. M. Sage, S. Sainis, T. Bergeman, and D. DeMille, Phys. Rev. Lett. **92**, 033004 (2004).
[10] D. Wang, E. E. Eyler, P. L. Gould, and W. C. Stwalley, Phys. Rev. A **72**, 032502 (2005).
[11] J. Sage, S. Sainis, T. Bergeman, and D. DeMille, Phys. Rev. Lett. **94**, 203001 (2005).
[12] O. Docenko, M. Tamanis, J. Zaharova, R. Ferber, A. Pashov, H. Knöckel, and E. Tiemann, J. Phys. B **39**, S929 (2006).
[13] F. Lang, K. Winkler, C. Strauss, R. Grimm, and J. Hecker Denschlag, Phys. Rev. Lett. **101**, 133005 (2008).
[14] C. R. Menegatti, B. S. Marangoni, and L. G. Marcassa, Laser Phys. **18**, 1305 (2008).
[15] K.-K. Ni, S. Ospelkaus, M. H. G. de Miranda, A. Péer, B. Neyenhuis, J. J. Zirbel, S. Kotochigova, P. Julienne, D. S. Jin, and J. Ye, Science **322**, 231 (2008).
[16] A.-C. Voigt, M. Taglieber, L. Costa, T. Aoki, W. Wieser, T. W. Hänsch, and K. Dieckmann, Phys. Rev. Lett. **102**, 020405 (2009).
[17] C. Haimberger, J. Kleinert, P. Zabawa, A. Wakim, and N. P. Bigelow, New J. Phys. **11**, 055042 (2009).
[18] J. T. Kim, D. Wang, E. E. Eyler, P. L. Gould, and W. C. Stwalley, New J. Phys. **11**, 055020 (2009).
[19] O. Dulieu and C. Gabbanini, Rep. Prog. Phys. **72**, 086401 (2009).
[20] A. Grochola, A. Pashov, J. Deiglmayr, M. Repp, E. Tiemann, R. Wester, and M. Weidemüller, J. Chem. Phys. **131**, 054304 (2009).
[21] D. J. McCabe, D. G. England, H. E. L. Martay, M. E. Friedman, J. Petrovic, E. Dimova, B. Chatel, and I. A. Walmsley, Phys. Rev. A **80**, 033404 (2009).
[22] S. Ospelkaus, K.-K. Ni, D. Wang, M. H. G. de Miranda, B. Neyenhuis, G. Quéméner, P. Julienne, J. L. Bohn, D. S. Jin, and J. Ye, Science **327**, 853 (2010).
[23] P. Zabawa, A. Wakim, A. Neukirch, C. Haimberger, N. P. Bigelow, A. V. Stolyarov, E. A. Pazyuk, M. Tamanis, and G. Ferrari, Phys. Rev. A **82**, 040501(R) (2010).
[24] K. Aikawa, D. Akamatsu, M. Hayashi, K. Oasa, J. Kobayashi, P. Naidon, T. Kishimoto, K. Ueda, and S. Inouye, Phys. Rev. Lett. **105**, 203001 (2010).
[25] N. Bouloufa, M. Pichler, M. Aymar, and O. Dulieu, Phys. Rev. A **83**, 022503 (2011).
[26] A. Grochola, P. Kowalczyk, J. Szczepkowski, W. Jastrzebski, A. Wakim, P. Zabawa, and N. P. Bigelow, Phys. Rev. A **84**, 012507 (2011).
[27] D. DeMille, Phys. Rev. Lett. **88**, 067901 (2002).
[28] D. DeMille and E. R. Hudson, Nat. Phys. **4**, 911 (2008).
[29] K. Mishima and K. Yamashita, Chem. Phys. **361**, 106 (2009).
[30] L. D. Carr, D. DeMille, R. V. Krems, and J. Ye, New J. Phys. **11**, 055049 (2009).
[31] M. Auzinsh, R. Ferber, O. Nikolayeva, N. Shafer-Ray, and M. Tamanis, J. Phys. D **34**, 624 (2001).
[32] M. Masters, J. Huennekens, W. T. Luh, Li Li, A. M. Lyyra, K. Sando, V. Zafiropulos, and W. C. Stwalley, J. Chem. Phys. **92**, 5801 (1990).
[33] H. Sun and J. Huennekens, J. Chem. Phys. **97**, 4714 (1992).
[34] Z. J. Jabbour and J. Huennekens, J. Chem. Phys. **107**, 1094 (1997).
[35] E. Laub, I. Mazsa, S. C. Webb, J. LaCivita, I. Prodan, Z. J. Jabbour, R. K. Namiotka, and J. Huennekens, J. Mol. Spectrosc. **193**, 376 (1999); erratum, *ibid.* **221**, 142 (2003).
[36] J. Huennekens, I. Prodan, A. Marks, L. Sibbach, E. Galle, T. Morgus, and Li Li, J. Chem. Phys. **113**, 7384 (2000).
[37] P. Burns, L. Sibbach-Morgus, A. D. Wilkins, F. Halpern, L. Clarke, R. D. Miles, Li Li, A. P. Hickman, and J. Huennekens, J. Chem. Phys. **119**, 4743 (2003).
[38] L. Morgus, P. Burns, R. D. Miles, A. D. Wilkins, U. Ogba, A. P. Hickman, and J. Huennekens, J. Chem. Phys. **122**, 144313 (2005).
[39] A. D. Wilkins, L. Morgus, J. Hernandez-Guzman, J. Huennekens, and A. P. Hickman, J. Chem. Phys. **123**, 124306 (2005).
[40] R. D. Miles, L. Morgus, D. O. Kashinski, J. Huennekens, and A. P. Hickman, J. Chem. Phys. **125**, 154304 (2006).
[41] P. Burns, A. D. Wilkins, A. P. Hickman, and J. Huennekens, J. Chem. Phys. **122**, 074306 (2005).
[42] S. Eckel, S. Ashman, and J. Huennekens, J. Mol. Spectrosc. **242**, 182 (2007).
[43] S. J. Sweeney, E. H. Ahmed, P. Qi, T. Kirova, A. M. Lyyra, and J. Huennekens, J. Chem. Phys. **129**, 154303 (2008).
[44] A. D. Wilkins, L. Morgus, J. Huennekens, and A. P. Hickman, J. Mol. Spectrosc. **258**, 13 (2009).
[45] B. M. McGeehan, S. Ashman, C. M. Wolfe, R. Steinhardt, M. L. Monaco, J. Huennekens, and A. P. Hickman, J. Mol. Spectrosc. **265**, 74 (2011).
[46] J. Deiglmayr, A. Grochola, M. Repp, O. Dulieu, R. Wester, and M. Weidemüller, Phys. Rev. A **82**, 032503 (2010).
[47] K. Onomichi and H. Katô, Bull. Chem. Soc. Jpn. **56**, 2577 (1983).
[48] U. Diemer, H. Weickenmeier, M. Wahl, and W. Demtröder, Chem. Phys. Lett. **104**, 489 (1984).
[49] O. Docenko, M. Tamanis, R. Ferber, A. Pashov, H. Knöckel, and E. Tiemann, Eur. Phys. J. D **31**, 205 (2004).
[50] J. Zaharova, M. Tamanis, R. Ferber, A. N. Drozdova, E. A. Pazyuk, and A. V. Stolyarov, Phys. Rev. A **79**, 012508 (2009).

[51]A. Pashov, W. Jastrzębski, and P. Kowalczyk, Comput. Phys. Commun. **128**, 622 (2000).
[52]N. W. Carlson, F. V. Kowalski, R. E. Teets, and A. L. Schawlow, Opt. Commun. **29**, 302 (1979).
[53]R. A. Bernheim, L. P. Gold, and T. Tipton, J. Chem. Phys. **78**, 3635 (1983).
[54]A. G. Astill, A. J. McCaffery, and B. J. Whitaker, Chem. Phys. Lett. **142**, 1 (1987).
[55]H. Wang, Li Li, A. M. Lyyra, and W. C. Stwalley, J. Mol. Spectrosc. **137**, 304 (1989).
[56]C.-C. Tsai, J. T. Bahns, T.-J. Whang, H. Wang, W. C. Stwalley, and A. M. Lyyra, Phys. Rev. Lett. **71**, 1152 (1993).
[57]G. Zhao, J. T. Kim, J. T. Bahns, and W. C. Stwalley, J. Mol. Spectrosc. **184**, 209 (1997).
[58]K. Urbanski, S. Antonova, A. M. Lyyra, Li Li, and B. Ji, J. Chem. Phys. **109**, 912 (1998).
[59]S. Antonova, G. Lazarov, K. Urbanski, A. M. Lyyra, Li Li, G.-H. Jeung, and W. C. Stwalley, J. Chem. Phys. **112**, 7080 (2000).
[60]S. Kasahara, P. Kowalczyk, M. H. Kabir, M. Baba, and H. Katô, J. Chem. Phys. **113**, 6227 (2000).
[61]M. H. Kabir, T. Shinano, and S. Kasahara, J. Chem. Phys. **118**, 7817 (2003).
[62]T.-J. Whang, H.-W. Wu, R.-Y. Chang, and C.-C. Tsai, J. Chem. Phys. **121**, 10513 (2004).
[63]A. J. Ross, F. Martin, A. Adohi-Krou, and C. Jungen, J. Mol. Spectrosc. **227**, 158 (2004).
[64]C. C. Tsai, R.-Y. Chang, and T. J. Whang, J. Mol. Spectrosc. **234**, 264 (2005).
[65]R.-Y. Chang, C. C. Tsai, T. J. Whang, and C.-P. Cheng, J. Chem. Phys. **123**, 224303 (2005).
[66]S. Kasahara, H. Ikoma, and H. Katô, J. Chem. Phys. **100**, 63 (1994).
[67]A. Pashov, I. Jackowska, W. Jastrzębski, and P. Kowalczyk, Phys. Rev. A **58**, 1048 (1998).
[68]N. H. Bang, W. Jastrzebski, and P. Kowalczyk, J. Mol. Spectrosc. **233**, 290 (2005).
[69]W. Jastrzebski, P. Kortyka, P. Kowalczyk, O. Docenko, M. Tamanis, R. Ferber, A. Pashov, H. Knöckel, and E. Tiemann, Eur. Phys. J. D **36**, 57 (2005).
[70]Li Li and R. W. Field, J. Phys. Chem. **87**, 3020 (1983).
[71]X. Xie and R. W. Field, J. Mol. Spectrosc. **117**, 228 (1986).
[72]G. Lazarov, A. M. Lyyra, and Li Li, J. Mol. Spectrosc. **205**, 73 (2001).
[73]D. Li, F. Xie, Li Li, A. Lazoudis, and A. M. Lyyra, J. Mol. Spectrosc. **246**, 180 (2007).
[74]Li Li, T. An, T.-J. Whang, A. M. Lyyra, W. C. Stwalley, R. W. Field, and R. A. Bernheim, J. Chem. Phys. **96**, 3342 (1992).
[75]A. Yiannopoulou, K. Urbanski, A. M. Lyyra, Li Li, B. Ji, J. T. Bahns, and W. C. Stwalley, J. Chem. Phys. **102**, 3024 (1995).
[76]Li Li, A. Yiannopoulou, K. Urbanski, A. M. Lyyra, B. Ji, W. C. Stwalley, and T. An, J. Chem. Phys. **105**, 6192 (1996); erratum, *ibid.* **106**, 8626 (1997).
[77]Li Li, A. Lazoudis, P. Yi, Y. Liu, J. Huennekens, R. W. Field, and A. M. Lyyra, J. Chem. Phys. **116**, 10704 (2002).
[78]Li Li and A. M. Lyyra, Spectrochim. Acta, Part A **55**, 2147 (1999).
[79]Li Li and R. W. Field, J. Mol. Spectrosc. **123**, 237 (1987).
[80]Li Li, Q. Zhu, and R. W. Field, J. Mol. Spectrosc. **134**, 50 (1989).
[81]T.-J. Whang, A. M. Lyyra, W. C. Stwalley, and Li Li, J. Mol. Spectrosc. **149**, 505 (1991).
[82]G. Lazarov, A. M. Lyyra, Li Li, and J. Huennekens, J. Mol. Spectrosc. **196**, 259 (1999).
[83]Y. Liu, B. Ji, A. S.-C. Cheung, W. C. Stwalley, R. W. Field, A. M. Lyyra, and Li Li, J. Chem. Phys. **115**, 3647 (2001).
[84]Y. Liu, Li Li, G. Lazarov, A. Lazoudis, A. M. Lyyra, and R. W. Field, J. Chem. Phys. **121**, 5821 (2004).
[85]P. Qi, G. Lazarov, A. M. Lyyra, Y. Liu, C. Cui, Li Li, and G.-H. Jeung, J. Chem. Phys. **124**, 184304 (2006).
[86]Li Li, A. M. Lyyra, W. T. Luh, and W. C. Stwalley, J. Chem. Phys. **93**, 8452 (1990).
[87]B. Ji, C.-C. Tsai, Li Li, T.-J. Whang, A. M. Lyyra, H. Wang, J. T. Bahns, W. C. Stwalley, and R. J. Le Roy, J. Chem. Phys. **103**, 7240 (1995).
[88]J. T. Kim, H. Wang, C. C. Tsai, J. T. Bahns, W. C. Stwalley, G. Jong, and A. M. Lyyra, J. Chem. Phys. **102**, 6646 (1995); erratum, *ibid.* **103**, 9891 (1995).
[89]J. Magnes, E. Ahmed, C. Goldberg, A. M. Lyyra, S. Magnier, M. Aubert-Frécon, Y. Liu, and Li Li, J. Mol. Spectrosc. **221**, 72 (2003).
[90]D. Li, F. Xie, Li Li, V. B. Sovkov, V. S. Ivanov, E. Ahmed, A. M. Lyyra, J. Huennekens, and S. Magnier, J. Chem. Phys. **126**, 194314 (2007).
[91]P. Kowalczyk, J. Chem. Phys. **91**, 2779 (1989).
[92]K. Ishikawa, T. Kumauchi, M. Baba, and H. Katô, J. Chem. Phys. **96**, 6423 (1992).
[93]Y.-C. Wang, K. Matsubara, and H. Katô, J. Chem. Phys. **97**, 811 (1992).
[94]S. Kasahara, T. Ebi, M. Tanimura, H. Ikoma, K. Matsubara, M. Baba, and H. Katô, J. Chem. Phys. **105**, 1341 (1996).
[95]C. Amiot, J. Mol. Spectrosc. **203**, 126 (2000).
[96]Y. T. Lee, Y. Yoon, and B. Kim, J. Chem. Phys. **120**, 6551 (2004).
[97]O. Docenko, M. Tamanis, R. Ferber, T. Bergeman, S. Kotochigova, A. V. Stolyarov, A. de Faria Nogueira, and C. E. Fellows, Phys. Rev. A **81**, 042511 (2010).
[98]C. M. Wolfe, S. Ashman, J. Bai, B. Beser, E. H. Ahmed, A. M. Lyyra, and J. Huennekens, J. Chem. Phys. **134**, 174301 (2011).
[99]See supplementary material at http://dx.doi.org/10.1063/1.3689388 for complete data tables.
[100]S. Gerstenkorn and P. Luc, *Atlas du Spectre D'Absorption de la Molécule D'Iode* (Centre National de la Recherche Scientifique, Paris, 1978).
[101]J. E. Sansonetti, W. C. Martin, and S. L. Young, *Handbook of Basic Atomic Spectroscopic Data*, version 1.1.2 (National Institute of Standards and Technology, Gaithersburg, MD, 2005); available online at http://physics.nist.gov/Handbook.
[102]R. Stair, W. E. Schneider, and J. K. Jackson, Appl. Opt. **2**, 1151 (1963).
[103]R. J. Le Roy, DParFit 3.3: A Computer Program for Fitting Diatomic Molecule Spectral Data to Parameterized Level Energy Expressions, University of Waterloo Chemical Physics Research Report No. CP-660, 2005, see http://leroy.uwaterloo.ca/programs/.
[104]S. T. Ashman, "Experimental studies of the NaCs $5^3\Pi_0$ and $1(a)^3\Sigma^+$ electronic states", Ph.D. dissertation (Lehigh University, 2010).
[105]R. J. Le Roy, RKR1 2.0: A Computer Program Implementing the First-Order RKR Method for Determining Diatomic Molecule Potential Energy Functions, University of Waterloo Chemical Physics Research Report CP-657R, 2004, see http://leroy.uwaterloo.ca/programs/.
[106]M. Korek, S. Bleik, and A. R. Allouche, J. Chem. Phys. **126**, 124313 (2007).
[107]H. Salami, T. Bergeman, B. Beser, J. Bai, E. Ahmed, S. Kotochigova, A. M. Lyyra, J. Huennekens, C. Lisdat, A. V. Stolyarov, O. Dulieu, P. Crozet, and A. J. Ross, Phys. Rev. A **80**, 022515 (2009).
[108]J. Bai, E. H. Ahmed, B. Beser, Y. Guan, S. Kotochigova, A. M. Lyyra, S. Ashman, C. M. Wolfe, J. Huennekens, F. Xie, D. Li, Li Li, M. Tamanis, R. Ferber, A. Drozdova, E. Pazyuk, A. V. Stolyarov, J. G. Danzl, H.-C. Nägerl, N. Bouloufa, O. Dulieu, C. Amiot, H. Salami, and T. Bergeman, Phys. Rev. A **83**, 032514 (2011).
[109]R. J. Le Roy and G. T. Kraemer, BCONT 2.2: A Computer Program for Calculating Bound → Continuum Transition Intensities for Diatomic Molecules, University of Waterloo Chemical Physics Research Report No. CP-650R, 2004, see http://leroy.uwaterloo.ca/programs/.
[110]M. Korek, S. Bleik, and A. R. Allouche (Ref. 106) identify the asymptotic limit of the NaCs $5^3\Pi_0$ state as Na($3P_{1/2}$)+Cs($6P_{1/2}$). However, we note that in their Table I listing the lowest dissociation limits, the final four entries should be Na($3S_{1/2}$)+Cs($5D_{3/2}$), Na($3S_{1/2}$)+Cs($5D_{5/2}$), Na($3S_{1/2}$)+Cs($8S_{1/2}$), and Na($4S_{1/2}$)+Cs($6S_{1/2}$) in order of energies. Thus the $5^3\Pi_0$ state, corresponding to the $12^{th}$ $0^+$ state, should adiabatically dissociate to the Na($3S_{1/2}$)+Na($5D_{5/2}$) limit.
[111]M. Aymar and O. Dulieu, Mol. Phys. **105**, 1733 (2007).
[112]C. H. Townes and A. L. Schawlow, *Microwave Spectroscopy* (McGraw-Hill, New York, 1955).
[113]E. Arimondo, M. Inguscio, and P. Violino, Rev. Mod. Phys. **49**, 31 (1977).
[114]H. Geisen, D. Neuschafer, and Ch. Ottinger, Z. Phys. D **4**, 263 (1987).
[115]R. J. Le Roy, LEVEL 8.0: A Computer Program for Solving the Radial Schrödinger Equation for Bound and Quasibound Levels, University of Waterloo Chemical Physics Research Report CP-663, 2007, see http://leroy.uwaterloo.ca/programs/.